The Astrophysical Journal, 756:76 (24pp), 2012 September 1 doi:10.1088/0004-637X/756/1/76


# GAS EMISSIONS IN PLANCK COLD DUST CLUMPS—A SURVEY OF THE $J = 1$–0 TRANSITIONS OF $^{12}$CO, $^{13}$CO, AND C$^{18}$O

Yuefang Wu[1], Tie Liu[1], Fanyi Meng[2], Di Li[3,4,5], Sheng-Li Qin[6], and Bing-Gang Ju[7,8]
[1] Department of Astronomy, Peking University, 100871 Beijing, China; ywu@pku.edu.cn
[2] Yuan Pei school, Peking University, 100871 Beijing, China
[3] National Astronomical Observatories, CAS, Chaoyang Dist., Datun Rd. A20, Beijing, China
[4] Space Science Institute, Boulder, CO, USA
[5] Jet Propulsion Laboratory, California Institute of Technology, Pasadena, CA, USA
[6] Physikalisches Institut, Universität zu Köln, Zülpicher Str. 77, 50937
[7] Purple Mountain Observatory, Qinghai Station, 817000, Delingha, China
[8] Key Laboratory for Radio Astronomy, CAS
*Received 2012 February 3; accepted 2012 June 21; published 2012 August 17*

## ABSTRACT

A survey toward 674 Planck cold clumps of the Early Cold Core Catalogue (ECC) in the $J = 1$–0 transitions of $^{12}$CO, $^{13}$CO, and C$^{18}$O has been carried out using the Purple Mountain Observatory 13.7 m telescope. Six hundred seventy-three clumps were detected with $^{12}$CO and $^{13}$CO emission, and 68% of the sample has C$^{18}$O emission. Additional velocity components were also identified. A close consistency of the three line peak velocities was revealed for the first time. Kinematic distances are given for all the velocity components, and half of the clumps are located within 0.5 and 1.5 kpc. Excitation temperatures range from 4 to 27 K, slightly larger than those of $T_d$. Line width analysis shows that the majority of ECC clumps are low-mass clumps. Column densities $N_{\rm H_2}$ span from $10^{20}$ to $4.5 \times 10^{22}$ cm$^{-2}$ with an average value of $(4.4 \pm 3.6) \times 10^{21}$ cm$^{-2}$. $N_{\rm H_2}$ cumulative fraction distribution deviates from the lognormal distribution, which is attributed to optical depth. The average abundance ratio of the $^{13}$CO to C$^{18}$O in these clumps is $7.0 \pm 3.8$, higher than the terrestrial value. Dust and gas are well coupled in 95% of the clumps. Blue profile asymmetry, red profile asymmetry, and total line asymmetry were found in less than 10% of the clumps, generally indicating that star formation is not yet developed. Ten clumps were mapped. Twelve velocity components and 22 cores were obtained. Their morphologies include extended diffuse, dense, isolated, cometary, and filament, of which the last is the majority. Twenty cores are starless, and only seven cores seem to be in a gravitationally bound state. Planck cold clumps are the most quiescent among the samples of weak red *IRAS*, infrared dark clouds, UC H II candidates, extended green objects, and methanol maser sources, suggesting that Planck cold clumps have expanded the horizon of cold astronomy.

*Key words:* dust, extinction – ISM: clouds – ISM: kinematics and dynamics – ISM: structure – stars: formation – stars: protostars

*Online-only material:* color figures, machine-readable tables

## 1. INTRODUCTION

Large samples significantly improve our understanding of star formation. At the beginning of star formation studies in the early 1970s, the Palomar Sky Survey (PSS) plates provided astronomers with optical-selected nebulae as targets of star-forming regions. The cataloged Sharpless H II regions (Sharpless 1959) from PSS served as sources for investigating gas and dust properties of molecular cloud complexes (Evans et al. 1977; Harvey et al. 1977). Nearby dark cores as well as cloud fragments were from Lynds dark nebula (Strom et al. 1975; Snell et al. 1980; Clark & Johnson 1981). With visual inspection, 70 small opaque sports were chosen for the surveys of low-mass cores with $^{13}$CO, C$^{18}$O, and $NH_3$, respectively (Myers et al. 1983; Myers & Benson 1983). A number of sources resulting from these earliest observations are still primary examples of low-mass star formation. However, the "optical dark" selection method is limited for probing star forming in deep molecular clouds. Bally & Lada (1983) chose infrared sources for detecting high velocity outflows in high-mass star formation regions. Particularly, *IRAS* point sources afforded plenty of samples for high-mass star formation regions. Based on the similar shapes of the far-infrared flux distribution of all embedded O-type stars, the *IRAS* color–color criteria were used to choose UC H II region candidates (Wood & Churchwell 1989) and further refined by molecular line studies (Cesaroni et al. 1992; Watson et al. 1997). Precursors of UC H II regions were also obtained from luminous *IRAS* sources and used for a number of surveys to examine the early characteristics of high-mass star formation (Molinari et al. 1996; Sridharan et al. 2002; Beuther et al. 2002; Wu et al. 2006). In recent years, earlier samples for high-mass star formation come from infrared dark clouds (IRDCs) surveyed by the *Midcourse Space Experiment* (*MSX*). These are extinction features against the bright mid-infrared background of the Galaxy (Egan et al. 1998). A number of starless massive cores were detected, which have narrower line widths and lower rotation temperatures than both UC H II region precursors and UC H II regions but have similar masses (Rathborne et al. 2006; Sridharan et al. 2005). However, *MSX* is limited to $|b| \leqslant 6^\circ$ of our Galaxy.

Now Planck surveys provide a wealth of early sources that are cold and have an unprecedented complete space distribution. The cold core Catalogue of Planck Objects (C3PO) includes 10,783 sources that are mainly cold clumps, intermediate structures of the fragmentation scenario. Their temperatures and densities range from 7 to 17 K and 30 to $10^5$ cm$^{-3}$, respectively, derived from the fluxes in the three highest frequency Planck bands (353, 545, 857 GHz) and the 3000 GHz of the *IRAS* band

(Planck Collaboration et al. 2011a). This enables us to probe the characteristics of the prestellar phase or starless clumps. The all-sky nature of the Planck cold clump sample is particularly useful for studying the global properties of Galactic star formation. A follow-up study with high-resolution observations by *Herschel* revealed extended regions of cold dust with color temperatures down to 11 K. The results show different evolutionary stages ranging from a quiescent, cold filament to clumps with star-formation activities (Juvela et al. 2010).

These known properties of Planck cold clumps currently were revealed with various bands of continuum emissions and only a set of eight C3PO sources selected from a different environment (Planck Collaboration et al. 2011b) were investigated with molecular lines. Examination with molecular lines is another essential aspect for understanding the properties of the Planck cold clumps. Molecular line studies of the Planck clumps, which are an unbiased sample of cold dust clumps in the Milky Way, will provide clues for probing a number of critical questions about clumps and star formation. What are the morphologies, physical parameters, and their variations in the Galaxy? What are the initial conditions of star formation, which we do not yet know? What are the dynamic factors in a variety of the clumps and is there any premonition of collapse? Is there any depletion and what are cold chemistry phenomena? In which environment can the cold clumps exist? What is the highest Galactic latitude where stars can form? CO is the most common tool for probing molecular regions. Although there is "dark gas" which is undetected in the available CO and H I surveys (Planck Collaboration et al. 2011c), CO is still a basic probe with which to address the above questions.

In this paper we report a survey of Planck cold clumps with $J = 1$–0 lines of $^{12}$CO and its major isotopes, $^{13}$CO and C$^{18}$O, using the telescope of the Purple Mountain Observatory (PMO) at Qinghai province in western China. Our target sources are chosen from the Early Cold Core Catalogue (ECC), which are the most reliable detections of C3PO clumps. Thus far we have surveyed 674 sources with single-point observations and mapped a subset of 10 clumps in different locations. In Section 2 the observations are described. In Section 3 we present the results. The discussions are given in Section 4 and a summary is given in Section 5.

## 2. OBSERVATIONS

Using the 13.7 m telescope of Qinghai Station of the PMO at De Ling Ha, the survey toward the ECC clumps with $^{12}$CO (1–0) and $^{13}$CO (1–0) lines was carried out from 2011 January to May. The half-power beam width at the 115 GHz frequency band is 56″. The pointing and tracking accuracies are better than 5″. The main beam efficiency is ∼50%. A newly installed SIS superconducting receiver with nine beam arrays was employed as the front end. The $^{12}$CO (1–0) line was observed at the upper sideband and the other two lines were observed simultaneously at the lower sideband. The typical system temperature ($T_{\rm sys}$) in single sideband mode is around 110 K and varies by about 10% for each beam. A fast Fourier transform spectrometer was used as the back end, with a total bandwidth of 1 GHz and 16,384 channels. The equivalent velocity resolution is 0.16 km s$^{-1}$ for the $^{12}$CO (1–0) line and 0.17 km s$^{-1}$ for the $^{13}$CO (1–0) and C$^{18}$O (1–0) lines, respectively. The position switch mode was adopted for single point observations. The off position for each "off" source was carefully chosen from an area within 3° of the "on" source, which has no or extremely weak CO emission based on the CO survey of the Milky Way (Dame et al. 1987, 2001). For those regions without CO data, we chose the off positions based on the *IRAS* 100 $\mu$m images. The integration time at the on/off position is 30 s.

We also mapped 10 sources that have rather strong CO emission. The On-The-Fly (OTF) observing mode was applied for mapping observations. The antenna continuously scanned a region of 22′ × 22′ centered on the Planck cold clumps with a scan speed of 20″ s$^{-1}$. The rms noise level was 0.2 K in the main beam antenna temperature $T_A^*$ for $^{12}$CO (1–0), and 0.1 K for $^{13}$CO (1–0) and C$^{18}$O (1–0). Since the edges of the OTF maps are rather noisy, only the central 14′ × 14′ regions are analyzed. The OTF data were then converted to three-dimensional (3D) cube data with a grid spacing of 30″. The IRAM software package GILDAS was used for the data reduction (Guilloteau & Lucas 2000).

## 3. RESULTS

To make the observation with a sufficiently high elevation for the 13.7 m telescope at De Ling Ha, our samples were chosen from the ECC with a decl. $\geqslant -20°$. There are 674 sources from the ECC that satisfy this criterion. The names and coordinates of the 674 clumps are listed in Table 1 (Columns 1–7). One clump marked with "∗∗" is without detection, and needs further checking. There are 36 clumps without suitable background reference positions for the CO emission observations, which are marked with "∗" after their names and are excluded from further analysis. Clumps with latitude higher than 25° are referred to as high latitude clumps. There are 41 high latitude clumps. According to Dame et al. (1987), the distributions of the detected clumps are assigned to different molecular complexes. The regions and corresponding longitude and latitude scopes are shown in Columns 1–3 of Table 2. The fourth column of Table 2 gives a number of clumps in each complex. Six hundred seventy-three clumps were detected to have the $^{12}$CO and $^{13}$CO emission, and 68% of the clumps have the C$^{18}$O emission. One hundred and eight additional velocity components were identified in both the $^{12}$CO and $^{13}$CO emission, 50% of which have C$^{18}$O emission. We made a Gaussian function fitting for each distinguishable velocity component of the spectral lines. The results of emissions and their physical parameters are presented in the following.

### 3.1. Emission Components and Characteristics of Line Profiles

Most of the observed clumps have a single velocity component in CO emission. Among the 673 sources, 123 have double velocity components and 16 have possible double velocity components; 18 have three velocity components and 10 have possible triple velocity components. Multiple components or blend emission were detected in 52 cold sources. The spectral line of each distinguishable component was fitted with a Gaussian function. Centroid velocity $V_{\rm lsr}$, antenna temperature $T_A^*$, and FWHM $\Delta V$ were obtained for all three CO lines, which are given in Table 3. Centroid velocity of $^{13}$CO was taken as the systemic velocity of each velocity component and listed in the second column of Table 4. Dense core masses are related to molecular line widths (Wang et al. 2009). We adopted an average value of $^{13}$CO line width of 1.3 km s$^{-1}$ for the nearby dark cores (Myers & Benson 1983) as a criterion to distinguish high-mass and low-mass clumps. If a clump contains one or more velocity components with a $^{13}$CO line width larger than 1.3 km s$^{-1}$, it is considered to be a candidate of high-mass clumps (group

**Table 1**
Surveyed ECC Clump Catalogue

| Name | Glon (°) | Glat (°) | R.A.(J2000) (h m s) | Decl.(J2000) (d m s) | R.A.(B1950) (h m s) | Decl.(B1950) (d m s) | Region |
|---|---|---|---|---|---|---|---|
| G001.38+20.94 | 1.3842772 | 20.941952 | 16 34 38.06 | −15 46 40.71 | 16 31 46.85 | −15 40 30.16 | Ophiuchus |
| G001.84+16.58 | 1.845703 | 16.587652 | 16 50 12.91 | −18 04 22.37 | 16 47 18.48 | −17 59 15.82 | Ophiuchus |
| G003.73+16.39 | 3.7353513 | 16.393143 | 16 55 21.78 | −16 43 35.31 | 16 52 28.86 | −16 38 50.32 | Ophiuchus |
| G003.73+18.30 | 3.7353513 | 18.308161 | 16 48 54.69 | −15 36 02.09 | 16 46 03.29 | −15 30 50.23 | Ophiuchus |
| G004.02+16.64 | 4.0209961 | 16.646044 | 16 55 10.45 | −16 21 23.27 | 16 52 17.98 | −16 16 37.51 | |
| G004.19+18.09 | 4.1967773 | 18.092196 | 16 50 42.47 | −15 22 25.13 | 16 47 51.29 | −15 17 20.75 | |
| G004.15+35.77 | 4.152832 | 35.777241 | 15 53 29.82 | −04 38 52.39 | 15 50 51.56 | −04 30 01.93 | High Glat |
| G004.17+36.67 | 4.1748047 | 36.678967 | 15 50 42.66 | −04 04 20.84 | 15 48 05.00 | −03 55 20.10 | High Glat |
| G004.41+15.90 | 4.4165034 | 15.907708 | 16 58 35.99 | −16 28 36.07 | 16 55 43.28 | −16 24 04.69 | |
| G004.46+16.64 | 4.4604487 | 16.646044 | 16 56 11.73 | −16 00 51.08 | 16 53 19.65 | −15 56 09.62 | |
| G004.54+36.74 | 4.5483394 | 36.748764 | 15 51 14.27 | −03 47 40.14 | 15 48 36.88 | −03 38 41.35 | High Glat |
| G004.81+37.02 | 4.8120112 | 37.028599 | 15 50 52.79 | −03 27 20.38 | 15 48 15.74 | −03 18 20.28 | High Glat |
| G004.92+17.95 | 4.9218745 | 17.954901 | 16 52 50.41 | −14 53 40.51 | 16 49 59.75 | −14 48 45.05 | |
| G005.03+19.07 | 5.0317378 | 19.076056 | 16 49 19.74 | −14 09 20.80 | 16 46 30.04 | −14 04 10.73 | |
| G005.29+11.07 | 5.2954097 | 11.072874 | 17 17 19.97 | −18 30 57.71 | 17 14 24.31 | −18 27 45.91 | |
| G005.29+14.47 | 5.2954097 | 14.477516 | 17 05 31.09 | −16 36 07.96 | 17 02 38.08 | −16 32 05.81 | |
| G005.31+10.78 | 5.3173823 | 10.78794 | 17 18 23.02 | −18 39 22.30 | 17 15 27.16 | −18 36 15.00 | |
| G005.69+36.84* | 5.6909175 | 36.84193 | 15 53 11.88 | −03 00 56.50 | 15 50 35.24 | −02 52 04.98 | High Glat |
| G005.80+19.92 | 5.8007808 | 19.926863 | 16 48 13.56 | −13 04 14.26 | 16 45 25.16 | −12 58 59.65 | |
| G006.08+20.26 | 6.0864253 | 20.264484 | 16 47 44.35 | −12 39 21.78 | 16 44 56.44 | −12 34 05.17 | |
| G006.04+36.74* | 6.04248 | 36.748764 | 15 54 10.81 | −02 50 56.32 | 15 51 34.33 | −02 42 08.46 | High Glat |
| G006.32+20.44 | 6.3281245 | 20.443523 | 16 47 40.85 | −12 22 03.36 | 16 44 53.28 | −12 16 46.52 | |
| G006.41+20.56 | 6.4160151 | 20.562996 | 16 47 28.67 | −12 13 52.53 | 16 44 41.26 | −12 08 34.85 | |
| G006.70+20.66 | 6.7016597 | 20.66263 | 16 47 46.71 | −11 57 20.05 | 16 44 59.61 | −11 52 03.63 | |
| G006.96+00.89 | 6.965332 | 0.895288 | 17 57 59.28 | −22 29 20.42 | 17 54 57.90 | −22 29 05.02 | Fourth quad |
| G006.94+05.84 | 6.9433589 | 5.8479061 | 17 39 41.49 | −19 58 05.07 | 17 36 43.62 | −19 56 29.92 | Fourth quad |
| G006.98+20.72 | 6.9873042 | 20.722441 | 16 48 12.55 | −11 42 10.17 | 16 45 25.73 | −11 36 55.55 | |
| G007.14+05.94 | 7.1411128 | 5.9416566 | 17 39 47.47 | −19 45 05.14 | 17 36 49.87 | −19 43 30.43 | Fourth quad |
| G007.53+21.10 | 7.5366206 | 21.101799 | 16 48 08.77 | −11 03 53.56 | 16 45 22.69 | −10 58 38.70 | |
| G007.80+21.10 | 7.8002925 | 21.101799 | 16 48 43.20 | −10 51 47.54 | 16 45 57.35 | −10 46 35.08 | |

(This table is available in its entirety in a machine-readable form in the online journal. A portion is shown here for guidance regarding its form and content.)

H), otherwise, it is taken as a candidate for low-mass clumps (group L). In some of the observed clumps, the spectral lines of the emission components depart from a Gaussian profile, which probably reflects the state of gas or originates from systematic motions and star formation activities. We classify the different non-Gaussian profiles with the following characters: $BA^+$: blue profile; $RA^+$: red profile; BA: blue asymmetric; RA: red asymmetric; De: possible depletion; BW: blue wing; RW: red wing; W: wings; P: pedestal; Dob: double components; T: three components; and M.B: multiple or blended components.

The normalized velocity difference $\delta V = (V_{\rm thick} - V_{\rm thin})/\delta V_{\rm thin}$ is applied to identify the blue and red profiles (Mardones et al. 1997), where $V_{\rm thick}$ is the peak velocity of $^{12}$CO (1–0), $V_{\rm thin}$ and $\delta V_{\rm thin}$ are the systemic velocity and the optical thin line width, respectively, of optically thin lines. We use $^{13}$CO (1–0) and C$^{18}$O (1–0) as the optically thin lines. If $\delta V < -0.25$, the line is classified as a "blue profile," and if $\delta V > 0.25$, the line is classified as a "red profile." The sources with blue or red profiles are listed in Table 5. We define $\delta V(12) = (V_{\rm thick} - V_{12})/\delta V_{\rm thin}$ to investigate line blue or red asymmetries where $\delta V_{12} < -0.25$ or $>0.25$, where $V_{12}$ is the center velocity of $^{12}$CO (1–0). The sources with asymmetric profiles are listed in Table 6. The spectrum characteristics are denoted in the last column of Table 3. Figure 1 presents the examples of the spectra of the $J = 1$–0 lines of the $^{12}$CO, $^{13}$CO, and C$^{18}$O with red, green, and blue colors, respectively, including single, double, and triple components and the characteristics of the spectral profiles.

### 3.2. Observed Parameters

The histograms of the line center (peak) velocity difference between the lines of $^{12}$CO and $^{13}$CO ($V_{12}$–$V_{13}$) and those of $^{13}$CO and C$^{18}$O ($V_{13}$–$V_{18}$) lines are shown in Figures 2(a) and (b). The distributions (blue solid histograms) of both the $V_{12} - V_{13}$ and $V_{13} - V_{18}$ are quite symmetric around the zero, and are fitted with a normal distribution (red curve). However, their distributions are much narrower than a standard normal distribution (red curve), but have a sharp peak at zero (see Figures 2(a) and (b)). Ninety-four percent of the clumps have $V_{12} - V_{13}$ less than $3\sigma$ of the velocity resolution (0.17 km s$^{-1}$) given by the spectrometer, and 98% of the clumps have $V_{13} - V_{18}$ less than $3\sigma$ of the velocity resolution. The velocity correlations between lines of $^{12}$CO–$^{13}$CO and $^{13}$CO–$^{18}$CO are shown in Figures 2(c) and (d). $Y = (1.002 \pm 0.001)X + (0.005 \pm 0.016)$ for $V_{12}$ ($Y$) to $V_{13}$ ($X$) and $Y = (0.992 \pm 0.005)X + (0.140 \pm 0.057)$ for $V_{13}$ ($Y$) to $V_{18}$ ($X$) show very good correlations and the correlation coefficient is 100%. This is the first time good agreement of the center velocities of the $^{12}$CO and its main isotopes, the $^{13}$CO and C$^{18}$O lines, has been shown with such a large sample. These results show that the peak velocities of the three CO lines agree very well, and demonstrate that they originate from the same emission regions. Comparisons of Figures 2(a) and (b) with Figures 2(c) and (d) show the agreement between $V_{\rm lsr}$ of the $^{13}$CO and C$^{18}$O lines is better than that of the $^{12}$CO and $^{13}$CO lines, which may suggest that the $^{12}$CO is easily affected by dynamic factors in the clump or its environment.

**Table 2**
Molecular Complexes Associated with the Cold Clumps

| Region | $l$ [°,°] | $b$ [°,°] | Number | $T_{12}$ (K) | $T_{13}$ (K) | $T_{18}$ (K) | FWHM(12) (km s$^{-1}$) | FWHM(13) (km s$^{-1}$) | FWHM(18) (km s$^{-1}$) | $N_{H_2}$ ($10^{21}$ cm$^{-2}$) | $T_{ex}$ (K) | $\tau$(13) | $X_{13}/X_{18}$ | $\sigma_{NT}$ (km s$^{-1}$) | $\sigma_{Therm}$ (km s$^{-1}$) | $\sigma_{3D}$ (km s$^{-1}$) |
|---|---|---|---|---|---|---|---|---|---|---|---|---|---|---|---|---|
| First quad | [12,100] | [−10,10] | 84 | 2.69(1.20) | 1.85(0.77) | 0.96(0.72) | 2.70(2.23) | 1.73(1.34) | 0.96(0.72) | 5.7(5.1) | 9.4(2.4) | 1.1(0.9) | 5.6(3.3) | 0.75(0.60) | 0.17(0.02) | 1.34(1.02) |
| Second quad | [98,180] | [−4,10] | 70 | 2.57(1.23) | 1.67(0.77) | 0.85(0.51) | 2.09(1.18) | 1.42(0.68) | 0.85(0.51) | 4.5(3.4) | 9.5(2.1) | 0.9(0.5) | 7.6(3.3) | 0.62(0.29) | 0.17(0.02) | 1.13(0.49) |
| Third quad | [180,279] | [−4,10] | 43 | 2.57(1.11) | 1.51(0.64) | 1.05(0.40) | 2.90(1.00) | 1.74(0.67) | 1.05(0.40) | 4.7(2.6) | 9.1(2.0) | 0.7(0.3) | 7.0(2.9) | 0.73(0.28) | 0.17(0.02) | 1.31(0.47) |
| Fourth quad and ctr | [300,15] | [−8,8] | 6 | 3.09(0.44) | 1.54(0.59) | 2.81(5.01) | 3.03(2.57) | 1.83(1.96) | 2.81(5.01) | 4.2(2.6) | 9.5(0.9) | 0.8(0.4) | 4.4(2.3) | 0.77(0.83) | 0.17(0.01) | 1.39(1.42) |
| Anticenter | [175,210] | [−9,7] | 16 | 2.95(0.85) | 1.90(0.77) | 0.80(0.44) | 2.63(1.09) | 1.47(0.61) | 0.80(0.44) | 4.7(2.1) | 9.3(1.7) | 0.9(0.3) | 7.6(1.1) | 0.67(0.24) | 0.17(0.02) | 1.20(0.39) |
| Aquila South | [27,40] | [−21,−10] | 2 | 4.69(0.65) | 2.78(0.63) | 0.34(0.03) | 0.83(0.16) | 0.58(0.09) | 0.34(0.03) | 3.1(0.4) | 12.8(1.3) | 0.9(0.1) | 9.0(0.2) | 0.24(0.04) | 0.20(0.01) | 0.54(0.05) |
| Cephens | [99,143] | [8,22] | 87 | 2.60(0.93) | 1.66(0.64) | 0.69(0.29) | 1.94(0.87) | 1.13(0.43) | 0.69(0.29) | 3.5(1.9) | 8.8(1.8) | 1.0(0.5) | 5.4(2.1) | 0.48(0.18) | 0.16(0.02) | 0.88(0.30) |
| High Glat | | $\lvert b\rvert \geqslant 25$ | 41 | 3.30(1.12) | 1.84(0.97) | 0.46(0.18) | 1.47(0.66) | 0.89(0.40) | 0.46(0.18) | 3.0(2.0) | 10.5(2.0) | 0.8(0.5) | 11.6(5.5) | 0.37(0.17) | 0.18(0.02) | 0.72(0.26) |
| Oph-Sgr | [8,40] | [9,24] | 9 | 3.23(1.49) | 2.11(1.08) | 0.42(0.16) | 1.30(0.46) | 0.81(0.29) | 0.42(0.16) | 3.0(1.6) | 10.2(2.7) | 0.9(0.5) | 6.1(2.9) | 0.34(0.13) | 0.18(0.02) | 0.67(0.20) |
| Ophiuchus | [344,4] | [7,25] | 6 | 5.84(0.56) | 3.89(0.40) | 0.42(0.11) | 1.10(0.23) | 0.70(0.16) | 0.42(0.11) | 5.9(2.0) | 15.0(1.2) | 1.1(0.1) | 7.0(5.6) | 0.29(0.07) | 0.21(0.01) | 0.63(0.10) |
| Orion | [180,225] | [−25,5] | 82 | 3.58(1.90) | 2.19(1.01) | 0.76(0.35) | 2.12(1.02) | 1.29(0.53) | 0.76(0.35) | 5.8(5.3) | 11.1(4.0) | 1.0(0.6) | 8.1(5.1) | 0.55(0.23) | 0.18(0.03) | 1.02(0.38) |
| Taurus | [152,180] | [−25,−3] | 153 | 3.15(1.32) | 2.08(0.86) | 0.62(0.26) | 1.67(0.78) | 1.07(0.42) | 0.62(0.26) | 4.2(2.9) | 10.3(2.6) | 1.0(0.7) | 6.2(3.4) | 0.45(0.18) | 0.18(0.02) | 0.85(0.29) |
| Other | | | 75 | 3.45(1.61) | 1.97(1.22) | 0.52(0.21) | 1.51(0.68) | 0.92(0.45) | 0.52(0.21) | 3.4(2.4) | 10.5(3.3) | 0.9(0.7) | 7.4(4.4) | 0.38(0.20) | 0.18(0.03) | 0.75(0.31) |

**Table 3**
Observed Line Parameters

| Name | $V_{lsr}(12)$ (km s$^{-1}$) | FWHM(12) (km s$^{-1}$) | $T_A(12)$ (K) | $V_{lsr}(13)$ (km s$^{-1}$) | FWHM(13) (km s$^{-1}$) | $T_A(13)$ (K) | $V_{lsr}(18)$ (km s$^{-1}$) | FWHM(18) (km s$^{-1}$) | $T_A(18)$ (K) | |
|---|---|---|---|---|---|---|---|---|---|---|
| G001.38+20.94 | 0.61(0.01) | 1.16(0.02) | 5.67(0.18) | 0.74(0.01) | 0.78(0.01) | 3.98(0.09) | 0.74(0.01) | 0.54(0.03) | 1.26(0.09) | |
| G001.84+16.58 | 6.05(0.01) | 1.32(0.03) | 5.58(0.17) | 5.87(0.01) | 0.69(0.01) | 4(0.09) | 5.87(0.01) | 0.38(0.02) | 1.67(0.09) | |
| G003.73+16.39 | 6.44(0.01) | 1.11(0.02) | 5.56(0.17) | 6.17(0.01) | 0.71(0.01) | 3.41(0.09) | 6.17(0.02) | 0.53(0.07) | 0.77(0.09) | RA |
| G003.73+18.30 | 4.44(0.01) | 1.36(0.02) | 6.68(0.21) | 4.37(0.01) | 0.97(0.01) | 4.34(0.08) | 4.32(0.01) | 0.43(0.02) | 2.45(0.08) | |
| G004.02+16.64 | 5.92(0.01) | 0.69(0.02) | 5.5(0.18) | 5.87(0) | 0.49(0.01) | 3.81(0.09) | 5.86(0.02) | 0.34(0.05) | 0.71(0.08) | |
| G004.19+18.09 | 3.64(0.01) | 1.63(0.02) | 5.94(0.19) | 3.5(0.01) | 1.23(0.01) | 4.12(0.09) | 3.73(0.02) | 0.44(0.05) | 0.94(0.08) | Dob |
| G004.19+18.09 | 6.68(0.01) | 0.88(0.02) | 6.63(0.19) | 6.69(0.01) | 0.62(0.01) | 3.16(0.09) | | | | |
| G004.15+35.77 | 2.47(0.01) | 1.92(0.03) | 4.72(0.14) | 2.61(0.01) | 1.06(0.02) | 3.17(0.09) | | | | |
| G004.17+36.67 | 2.55(0.01) | 0.93(0.02) | 5.08(0.17) | 2.47(0.01) | 0.71(0.01) | 3.27(0.08) | | | | |
| G004.41+15.90 | 4.78(0.01) | 0.57(0.01) | 6.11(0.15) | 4.73(0) | 0.48(0.01) | 3.69(0.09) | | | | |
| G004.46+16.64 | 5.16(0.01) | 1.66(0.02) | 6.1(0.15) | 5.34(0.01) | 1.19(0.02) | 3.67(0.09) | 5.55(0.01) | 0.43(0.03) | 1.42(0.09) | BA$^+$ |
| G004.54+36.74 | 2.46(0.01) | 1.17(0.02) | 4.5(0.17) | 2.53(0.01) | 0.76(0.02) | 2.94(0.09) | 2.54(0.04) | 0.44(0.1) | 0.44(0.09) | |
| G004.81+37.02 | 3.6(0.01) | 1.51(0.02) | 4.47(0.13) | 3.71(0.01) | 1.04(0.02) | 2.91(0.09) | 3.82(0.04) | 0.66(0.09) | 0.46(0.08) | |
| G004.92+17.95 | 3.54(0.02) | 1.49(0.03) | 3.77(0.18) | 3.72(0.01) | 0.63(0.03) | 3.26(0.17) | 3.71(0.01) | 0.32(0.03) | 0.98(0.08) | |
| G005.03+19.07 | 3.83(0.01) | 1.25(0.02) | 7.17(0.19) | 3.77(0.01) | 0.99(0.01) | 3.86(0.09) | 3.81(0.03) | 0.65(0.07) | 0.73(0.09) | |
| G005.29+11.07 | 4.37(0.01) | 0.92(0.01) | 7.55(0.18) | 4.22(0) | 0.63(0.01) | 4.07(0.09) | 4.14(0.01) | 0.34(0.04) | 1.16(0.09) | |
| G005.29+14.47 | 3.76(0.01) | 0.4(0.01) | 5.07(0.18) | 3.74(0.01) | 0.3(0.02) | 1.21(0.09) | | | | |
| G005.31+10.78 | 4.53(0.01) | 1.24(0.02) | 6.56(0.19) | 4.38(0.01) | 0.88(0.01) | 4.1(0.1) | | | | |
| G005.69+36.84 | 0.56(0.03) | 1.39(0.06) | 3.84(0.17) | 0.6(0.03) | 0.96(0.07) | 0.81(0.09) | | | | Dob |
| G005.69+36.84 | 2.25(0.04) | 1.62(0.08) | 3.4(0.17) | 2.33(0.01) | 0.9(0.02) | 3.01(0.09) | 2.27(0.01) | 0.4(0.02) | 1.46(0.09) | |
| G005.80+19.92 | 3.45(0.01) | 1.41(0.02) | 6.11(0.18) | 3.06(0.01) | 0.89(0.01) | 3.87(0.09) | 2.96(0.02) | 0.47(0.05) | 0.99(0.09) | |
| G006.08+20.26 | 4.03(0.01) | 1.95(0.02) | 5.23(0.16) | 3.96(0.01) | 0.91(0.01) | 4.19(0.08) | 3.97(0.01) | 0.56(0.03) | 1.16(0.08) | BA$^+$ |
| G006.04+36.74 | 2.34(0.02) | 1.99(0.04) | 3.61(0.17) | 2.61(0.01) | 0.94(0.02) | 2.73(0.1) | 2.53(0.01) | 0.47(0.03) | 1.47(0.09) | |
| G006.32+20.44 | 4.48(0.01) | 1.6(0.02) | 4.98(0.16) | 4.32(0.01) | 0.72(0.01) | 4.25(0.09) | 4.27(0.01) | 0.38(0.02) | 1.88(0.09) | |
| G006.41+20.56 | 4.54(0.01) | 1.38(0.02) | 5.9(0.16) | 4.39(0.01) | 0.95(0.01) | 4.43(0.08) | 4.44(0.02) | 0.67(0.04) | 1.37(0.09) | |
| G006.70+20.66 | 3.49(0.01) | 2(0.03) | 4.44(0.15) | 3.76(0.01) | 1.06(0.01) | 3.97(0.08) | 3.79(0.01) | 0.66(0.04) | 1.35(0.09) | |
| G006.96+00.89 | 9.78(0.05) | 4.1(0.12) | 2.66(0.23) | 9.33(0.05) | 2.17(0.15) | 0.88(0.1) | | | | Dob |
| G006.96+00.89 | 41.34(0.06) | 9.42(0.15) | 3.11(0.23) | 41.53(0.1) | 6.89(0.24) | 0.77(0.1) | 41.67(0.63) | 13.03(2.05) | 0.17(0.1) | |
| G006.94+05.84 | 5.22(0.02) | 1.57(0.04) | 3.26(0.19) | 4.86(0.02) | 0.63(0.06) | 1.21(0.1) | | | | Dob |
| G006.94+05.84 | 10.59(0.02) | 2.57(0.05) | 3.38(0.19) | 10.08(0.02) | 1.39(0.03) | 2.22(0.1) | 10.05(0.03) | 0.83(0.07) | 0.77(0.09) | |

(This table is available in its entirety in a machine-readable form in the online journal. A portion is shown here for guidance regarding its form and content.)

**Table 4**
Derived Parameters of Surveyed ECC Clumps

| Name | $V_{lsr}$ (km s$^{-1}$) | $R$ (kpc) | $D$ (kpc) | $Z$ (kpc) | $T_{ex}$ (K) | $\tau(13)$ | $N(13)$ ($10^{15}$ cm$^{-2}$) | $\tau(18)$ | $N(18)$ ($10^{15}$ cm$^{-2}$) | $N_{H_2}$ ($10^{21}$ cm$^{-2}$) | Ratio(12/13) | $X_{13}/X_{18}$ (km s$^{-1}$) | $\sigma_{NT}$ (km s$^{-1}$) | $\sigma_{Therm}$ (km s$^{-1}$) | $\sigma_{3D}$ |
|---|---|---|---|---|---|---|---|---|---|---|---|---|---|---|---|
| G001.38+20.94 | 0.74 | 7.47 | 1.1 | 0.39 | 14.8 | 1.2 | 7.3 | 0.2 | 1.6 | 6.5 | 2.1 | 4.6 | 0.32 | 0.21 | 0.67 |
| G001.84+16.58 | 5.87 | 4.51 | 4.16 | 1.19 | 14.6 | 1.2 | 6.5 | 0.4 | 1.5 | 5.7 | 2.7 | 4.3 | 0.29 | 0.21 | 0.61 |
| G003.73+16.39 | 6.17 | 5.87 | 2.75 | 0.78 | 14.6 | 0.9 | 5.7 | 0.1 | 1.0 | 5.0 | 2.5 | 5.9 | 0.29 | 0.21 | 0.63 |
| G003.73+18.30 | 4.32 | 6.48 | 2.14 | 0.67 | 16.8 | 1.0 | 10.6 | 0.5 | 2.7 | 9.4 | 2.2 | 4.0 | 0.41 | 0.23 | 0.80 |
| G004.02+16.64 | 5.86 | 6.10 | 2.52 | 0.72 | 14.4 | 1.2 | 4.3 | 0.1 | 0.6 | 3.9 | 2.0 | 7.7 | 0.20 | 0.21 | 0.50 |
| G004.19+18.09 | 3.73 | 6.88 | 1.71 | 0.53 | 15.3 | 1.2 | 12.1 | 0.2 | 1.0 | 10.8 | 1.9 | 12.2 | 0.52 | 0.22 | 0.97 |
| G004.19+18.09 | 6.69 | 5.92 | 2.73 | 0.85 | 16.7 | 0.6 | 4.9 | | | 4.4 | 3.0 | | 0.25 | 0.23 | 0.59 |
| G004.15+35.77 | 2.61 | 7.13 | 1.7 | 0.99 | 12.9 | 1.1 | 7.4 | | | 6.6 | 2.7 | | 0.45 | 0.20 | 0.85 |
| G004.17+36.67 | 2.47 | 7.19 | 1.64 | 0.98 | 13.6 | 1.0 | 5.2 | | | 4.7 | 2.0 | | 0.29 | 0.20 | 0.62 |
| G004.41+15.90 | 4.73 | 6.62 | 1.96 | 0.54 | 15.7 | 0.9 | 4.3 | | | 3.8 | 2.0 | | 0.19 | 0.22 | 0.50 |
| G004.46+16.64 | 5.55 | 6.37 | 2.23 | 0.64 | 15.6 | 0.9 | 10.6 | 0.3 | 1.5 | 9.4 | 2.3 | 7.1 | 0.50 | 0.22 | 0.95 |
| G004.54+36.74 | 2.54 | 7.25 | 1.56 | 0.93 | 12.4 | 1.0 | 4.9 | 0.1 | 0.4 | 4.3 | 2.4 | 11.5 | 0.32 | 0.19 | 0.64 |
| G004.81+37.02 | 3.82 | 6.79 | 2.15 | 1.30 | 12.3 | 1.0 | 6.6 | 0.1 | 0.7 | 5.9 | 2.2 | 9.9 | 0.44 | 0.19 | 0.83 |
| G004.92+17.95 | 3.71 | 7.10 | 1.48 | 0.46 | 10.9 | 2.0 | 4.3 | 0.3 | 0.7 | 3.8 | 2.7 | 6.5 | 0.26 | 0.18 | 0.55 |
| G005.03+19.07 | 3.81 | 7.08 | 1.5 | 0.49 | 17.8 | 0.8 | 9.9 | 0.1 | 1.2 | 8.8 | 2.3 | 8.0 | 0.41 | 0.23 | 0.82 |
| G005.29+11.07 | 4.14 | 7.09 | 1.44 | 0.28 | 18.6 | 0.8 | 6.8 | 0.2 | 1.1 | 6.1 | 2.7 | 6.5 | 0.26 | 0.24 | 0.61 |
| G005.29+14.47 | 3.74 | 7.20 | 1.35 | 0.34 | 13.6 | 0.3 | 0.8 | | | 0.7 | 5.6 | | 0.11 | 0.20 | 0.40 |
| G005.31+10.78 | 4.38 | 7.03 | 1.51 | 0.28 | 16.6 | 1.0 | 9.0 | | | 8.0 | 2.3 | | 0.37 | 0.22 | 0.75 |
| G005.69+36.84 | 0.6 | 8.33 | 0.21 | 0.13 | 11.1 | 0.2 | 1.6 | | | 1.4 | 6.9 | | 0.40 | 0.18 | 0.77 |
| G005.69+36.84 | 2.27 | 7.60 | 1.13 | 0.68 | 10.2 | 2.1 | 5.5 | 0.6 | 1.2 | 4.9 | 2.0 | 4.6 | 0.38 | 0.18 | 0.72 |
| G005.80+19.92 | 2.96 | 7.52 | 1.05 | 0.36 | 15.7 | 1.0 | 8.3 | 0.2 | 1.1 | 7.4 | 2.5 | 7.4 | 0.37 | 0.22 | 0.75 |
| G006.08+20.26 | 3.97 | 7.26 | 1.33 | 0.46 | 13.9 | 1.6 | 8.7 | 0.2 | 1.5 | 7.7 | 2.7 | 5.9 | 0.38 | 0.21 | 0.75 |

(This table is available in its entirety in a machine-readable form in the online journal. A portion is shown here for guidance regarding its form and content.)

**Table 5**
Sources with Blue or Red Line Profiles

| Name | $V_{13}$ (km s$^{-1}$) | FWHM13 (km s$^{-1}$) | $V_{18}$ (km s$^{-1}$) | FWHM18 (km s$^{-1}$) | V12_peak (km s$^{-1}$) | $\delta V\_13$[a] | $\delta V\_18$[b] | T12_B/T12_R | $\Delta T$[c] | Profile | Region |
|---|---|---|---|---|---|---|---|---|---|---|---|
| G004.46+16.64 | 5.34(0.01) | 1.19(0.02) | 5.55(0.01) | 0.43(0.03) | 4.95 | −0.33 | −1.40 | 1.42 | 1.88 | Blue profile | Others |
| G006.08+20.26 | 3.96(0.01) | 0.91(0.01) | 3.97(0.01) | 0.56(0.03) | 3.25 | −0.78 | −1.29 | 1.09 | 0.42 | Blue profile | Others |
| G089.03−41.28 | −4.63(0.03) | 1.93(0.06) | | | −5.37 | −0.38 | 0.63 | 1.23 | 0.63 | Blue profile | High Glat |
| G097.09+10.12 | −2.71(0.03) | 1.09(0.05) | −2.67(0.04) | 0.63(0.09) | −3.33 | −0.57 | −1.05 | 1.57 | 1.01 | Blue profile | Others |
| G111.33+19.94 | −7.21(0.01) | 0.83(0.03) | −7.24(0.02) | 0.58(0.05) | −8.13 | −1.11 | −1.53 | 1.21 | 0.5 | Blue profile | Cephens |
| G111.77+13.78 | −3.81(0.01) | 0.85(0.03) | −3.68(0.05) | 0.46(0.15) | −4.29 | −0.56 | −1.33 | 2.18 | 1.69 | Blue profile | Cephens |
| G111.77+20.26 | −8.06(0.01) | 1.15(0.03) | −8.09(0.04) | 0.88(0.11) | −8.62 | −0.49 | −0.60 | 1.84 | 1.55 | Blue profile | Cephens |
| G111.97+20.52 | −7.92(0.02) | 0.9 (0.05) | −7.91(0.03) | 0.48(0.08) | −8.62 | −0.78 | −1.48 | 1.69 | 0.86 | Blue profile | Cephens |
| G117.11+12.42 | 3.87(0.01) | 0.96(0.03) | 3.92(0.02) | 0.53(0.06) | 3.32 | −0.57 | −1.13 | 1.25 | 0.78 | Blue profile | Cephens |
| G126.49−01.30 | −11.94(0.02) | 1.9 (0.04) | −11.74(0.04) | 0.91(0.09) | −13 | −0.56 | −1.38 | 1.19 | 0.6 | Blue profile | Second quad |
| G130.14+13.78 | −1.53(0.02) | 1.46(0.06) | −1.43(0.05) | 0.69(0.14) | −2.55 | −0.70 | −1.62 | 1.11 | 0.23 | Blue profile | Cephens |
| G155.45−14.59 | 1.97(0.02) | 1.39(0.05) | 2.13(0.03) | 0.61(0.1) | 0.83 | −0.82 | −2.13 | 2.50 | 1.93 | Blue profile | Taurus |
| G158.37−20.72 | 7.13(0.01) | 2.35(0.02) | 7.05(0.03) | 1.4(0.08) | 6.03 | −0.47 | −0.73 | 1.11 | 0.80 | Blue profile | Taurus |
| G164.94−08.57 | −0.7(0.01) | 1.71(0.03) | −0.63(0.05) | 1.31(0.11) | −1.66 | −0.56 | −0.79 | 1.73 | 1.89 | Blue profile | Taurus |
| G181.84+00.31 | 3.3(0.02) | 1.49(0.04) | 3.49(0.05) | 0.81(0.12) | 2.21 | −0.73 | −1.58 | 1.29 | 0.74 | Blue profile | Third quad |
| G190.17−13.78 | 1.14(0.01) | 1.39(0.02) | | | 0.74 | −0.29 | | 1.12 | 0.54 | Blue profile | Orion |
| G210.01−20.16 | 8.1(0.02) | 1.83(0.04) | 8.33(0.09) | 0.68(0.22) | 7.27 | −0.45 | −1.56 | 1.25 | 0.99 | Blue profile | Orion |
| G224.27−00.82 | 14.39(0.02) | 3.04(0.04) | 14.45(0.02) | 1.61(0.05) | 13.09 | −0.43 | −0.84 | 1.28 | 0.7 | Blue profile | Third Quad |
| G093.22−04.59 | 3.87(0.01) | 1.51(0.03) | 3.9(0.06) | 1.14(0.15) | 4.41 | 0.36 | 0.45 | 1.1 | 0.29 | Red profile | First quad |
| G101.14−15.28 | −9.58(0.01) | 0.98(0.03) | | | −9.18 | 0.41 | 0.29 | 0.92 | 0.29 | Red profile | Others |
| G121.92−01.71 | −14.07(0.01) | 1.39(0.03) | −14.12(0.08) | 1.11(0.16) | −13.46 | 0.44 | 0.59 | 0.87 | 0.5 | Red profile | Second quad |
| G145.81+10.97 | −14.94(0.02) | 1.06(0.04) | | | −14.31 | 0.59 | 0.29 | 0.90 | 0.29 | Red profile | Others |
| G157.10−08.70 | −7.48(0.02) | 1.43(0.04) | −7.48(0.03) | 0.9(0.08) | −6.98 | 0.35 | −1.40 | 0.55 | 1.8 | Red profile | Taurus |
| G169.84−07.61 | 6.46(0.01) | 0.67(0.02) | 6.39(0.01) | 0.31(0.03) | 6.83 | 0.55 | 1.42 | 0.90 | 0.35 | Red profile | Taurus |
| G172.85+02.27 | −17.22(0.02) | 3.18(0.06) | −17.49(0.07) | 1.47(0.17) | −15.83 | 0.44 | 1.13 | 0.90 | 0.45 | Red profile | Second quad |
| G182.15−17.95 | 9.4(0.01) | 0.86(0.02) | 9.35(0.03) | 0.53(0.06) | 10.11 | 0.83 | −0.64 | 0.71 | 1.26 | Red profile | Orion |
| G182.54−25.34 | 1.06(0.05) | 1.45(0.1) | | | 1.78 | 0.50 | 0.87 | 0.74 | 0.87 | Red profile | High Glat |
| G188.04−03.71 | 3.12(0.03) | 1.39(0.06) | 3.15(0.08) | 0.9(0.16) | 4.03 | 0.65 | −1.02 | 0.73 | 0.52 | Red profile | Third quad |
| G192.28−11.33 | 10.19(0.01) | 1.47(0.01) | 10.13(0.04) | 0.84(0.11 | 10.81 | 0.42 | 0.81 | 0.75 | 1.61 | Red profile | Orion |
| G195.09−16.41 | −0.08(0.01) | 1.84(0.02) | −0.1(0.05) | 1.3(0.13) | 0.47 | 0.30 | −0.47 | 0.89 | 0.77 | Red profile | Orion |
| G210.67−36.77 | 0.47(0.01) | 0.6(0.02) | 0.45(0.06) | 0.24(0.09) | 0.81 | 0.57 | 1.50 | 0.84 | 0.93 | Red profile | High Glat |
| G216.69−13.88 | 8.72(0.02) | 1.88(0.06) | 8.81(0.07) | 0.8(0.13) | 9.71 | 0.53 | 1.13 | 0.91 | 0.32 | Red profile | Orion |
| G219.35−09.70 | 12.5(0.02) | 1.65(0.04) | 12.45(0.03) | 0.93(0.07) | 13.41 | 0.55 | 1.03 | 0.67 | 0.76 | Red profile | Orion |

**Notes.**
[a] $\delta V\_13$ = (V12_peak-V13)/FWHM13.
[b] $\delta V\_18$ = (V12_peak-V18)/FWHM18.
[c] $\Delta T$ = abs(T12_b-T12_r).

Since there are fewer sources in which $C^{18}O$ lines were detected compared with those in which $^{13}CO$ lines were detected, we adopt the center velocity of $^{13}CO$ as the systemic velocity of the clumps in the following analysis. For the components without $^{13}CO$ (1–0) emission, the center velocities of $^{12}CO$ were adopted as the systemic velocity.

The main beam antenna temperatures of the three transitions for all the components detected were obtained. $T_{12}$ ranges from 0.5 to 12 K. The three clumps G209.28−19.62 (12 K), G192.54−11.56 (9.2 K), and G207.35−19.82 (8.8 K), temperatures which are all located in the Orion region, have the highest. Generally, the antenna temperatures of $^{13}CO$ and $C^{18}O$ are also high in the $^{12}CO$ emission strong clumps. For the above three clumps, $T_{13}$ and $T_{18}$ are 6.8, 1.4; 5.0, 0.6; and 3.1, 0.4 K, respectively. The ratio of $T_{12}/T_{13}$ is between 2.8 and 1.8, showing that the $^{12}CO$ line emissions have large opacity. The ratio of $T_{13}/T_{18}$ ranges between 4.5 and 8.3, with an average value of 6.0 which is close to the terrestrial value. However, the ratio may be different in different regions, for example, in the Ophiuchus complex, the antenna temperatures of the three transitions are 6.7, 4.4, and 2.5 K for G003.73+18.30 and 5.9, 4.4, and 1.4 K for G006.41+20.56. The ratio of $T_{13}/T_{18}$ is 1.8 and 3.1 for the two clumps, respectively, which is much less than 5.5, suggesting that the $^{13}CO$ lines are optically thick. For all the detected components, the histograms of $T_{12}$ and the ratios of $T_{12}/T_{13}$ and $T_{13}/T_{18}$ are present in Figures 3(a)–(c), respectively. The peak of $T_{12}$ is around 3 K. For the ratio of $T_{12}/T_{13}$, the mean value is 2.2 with a standard deviation of 1.4, showing that the $^{12}CO$ (1–0) line emissions of the cold clumps are generally optically thick. The mean value of the ratio of $T_{13}/T_{18}$ is 3.9 with a standard deviation of 1.7.

We found that all the distributions of the observed parameters as well as the derived parameters seemed to skew to the right with a long tail at the high value side. We try to depict their distributions with a lognormal distribution. The probability density function (PDF) of a lognormal distribution is

$$f_X(x;\mu,\sigma) = \frac{1}{x\sigma(2\pi)^{1/2}} e^{-\frac{(\ln x-\mu)^2}{2\sigma^2}}, \quad x > 0, \qquad (1)$$

where $x$ is the value of the variable, the parameters $\mu$ and $\sigma$ are the mean and standard deviation, respectively, of the variable's natural logarithm. The Kolmogorov-Smirnov test (K-S test) is applied to identify whether the parameters follow a lognormal

**Table 6**
Sources with Blue or Red Line Asymmetry

| Name | FWHM13 (km s$^{-1}$) | FWHM18 (km s$^{-1}$) | $V_{12}$ (km s$^{-1}$) | V12_peak (km s$^{-1}$) | $\delta V(12)\_13$[a] | $\delta V(12)\_18$[b] | Profile | Region |
|---|---|---|---|---|---|---|---|---|
| G018.39+19.39 | 0.52(0.01) | 0.27(0.04) | −0.46(0.01) | −0.61 | −0.29 | −0.56 | Blue asymmetry | Oph-Sgr |
| G027.70−21.02 | 0.47(0.04) | | 4.95(0.02) | 4.78 | −0.36 | | Blue asymmetry | |
| G108.10+13.19 | 1.04(0.04) | 0.43(0.03) | −4.81(0.03) | −5.17 | −0.35 | −0.84 | Blue asymmetry | Cephens |
| G111.66+20.20 | 1.34(0.03) | 0.79(0.09) | −8.17(0.03) | −8.64 | −0.35 | −0.59 | Blue asymmetry | Cephens |
| G143.85+11.49 | 1.63(0.08) | | −13.78(0.06) | −14.3 | −0.32 | | Blue asymmetry | Others |
| G147.96−08.02 | 0.63(0.1) | | −28.39(0.04) | −28.59 | −0.32 | | Blue asymmetry | Others |
| G156.90−08.49 | 1.92(0.06) | 0.53(0.05) | −7.72(0.04) | −8.56 | −0.44 | −1.58 | Blue asymmetry | Taurus |
| G158.24−21.80 | 1.63(0.03) | 1.13(0.13) | 4.09(0.02) | 3.45 | −0.39 | −0.57 | Blue asymmetry | Taurus |
| G158.40−21.86 | 1.21(0.03) | 0.92(0.1) | 4.54(0.01) | 4.13 | −0.34 | −0.45 | Blue asymmetry | Taurus |
| G159.65+11.39 | 1.11(0.02) | 0.99(0.27) | 2.61(0.01) | 1.9 | −0.64 | −0.72 | Blue asymmetry | Others |
| G171.43−17.36 | 1.16(0.02) | 0.4(0.03) | 7.47(0.02) | 6.99 | −0.41 | −1.20 | Blue asymmetry | Taurus |
| G172.92−16.74a | 0.7(0.02) | 0.51(0.08) | 5.06(0.02) | 4.9 | −0.23 | −0.31 | Blue asymmetry? | Taurus |
| G172.92−16.74b | 0.87(0.02) | 0.58(0.05) | 6.96(0.02) | 6.49 | −0.54 | −0.81 | Blue asymmetry | Taurus |
| G173.18−09.12 | 0.5(0.02) | 0.51(0.09) | 6.23(0.02) | 6.03 | −0.40 | −0.39 | Blue asymmetry | Taurus |
| G179.14−06.27 | 0.52(0.02) | | 7.69(0.02) | 7.45 | −0.46 | | Blue asymmetry | Anticenter |
| G182.02−00.16 | 1.28(0.05) | 0.89(0.18) | 3.91(0.02) | 3.43 | −0.38 | −0.54 | Blue asymmetry | Third quad |
| G190.08−13.51 | 1.62(0.03) | | 1.11(0.02) | 0.64 | −0.29 | | Blue asymmetry | Orion |
| G196.21−15.50 | 2.29(0.08) | | 3.51(0.02) | 2.88 | −0.28 | | Blue asymmetry | Orion |
| G227.70+11.18 | 0.59(0.14) | | 14.98(0.02) | 14.78 | −0.34 | | Blue asymmetry | Others |
| G003.73+16.39 | 0.71(0.01) | 0.53(0.07) | 6.44(0.01) | 6.67 | 0.32 | 0.43 | Red asymmetry | Ophiuchus |
| G118.34+08.66 | 0.72(0.05) | 0.41(0.14) | −2.07(0.03) | −1.79 | 0.39 | 0.68 | Red asymmetry | Cephens |
| G118.36+21.74 | 0.86(0.06) | | −3.88(0.04) | −3.5 | 0.44 | | Red asymmetry | Cephens |
| G142.25+05.43 | 0.97(0.03) | | −10.18(0.01) | −9.85 | 0.34 | | Red asymmetry | Second quad |
| G142.62+07.29 | 0.66(0.03) | 0.36(0.11) | −11.42(0.02) | −10.97 | 0.68 | 1.25 | Red asymmetry | Second quad |
| G157.19−08.81 | 1.29(0.03) | 0.74(0.06) | −7(0.02) | −6.49 | 0.40 | 0.69 | Red asymmetry | Taurus |
| G157.25−01.00 | 0.67(0.01) | 0.36(0.02) | 5.27(0.01) | 5.5 | 0.34 | 0.64 | Red asymmetry | Second quad |
| G157.58−08.89 | 1.07(0.04) | 0.41(0.03) | −6.07(0.03) | −5.37 | 0.65 | 1.71 | Red asymmetry | Taurus |
| G159.58−32.84 | 1.38(0.07) | | 3.79(0.02) | 4.43 | 0.46 | | Red asymmetry | High Glat |
| G174.50−19.88 | 0.81(0.02) | 0.56(0.09) | 7.7(0.01) | 7.96 | 0.32 | 0.46 | Red asymmetry | Taurus |
| G175.16−16.74 | 1.11(0.03) | 0.8(0.1) | 5.7(0.03) | 6.23 | 0.48 | 0.66 | Red asymmetry | Second quad |
| G195.00−16.95 | 1.1(0.02) | 0.51(0.04) | −1.99(0.01) | −1.76 | 0.21 | 0.45 | Red asymmetry | Orion |
| G221.46−17.89 | 0.46(0.03) | 0.17(0.66) | 7.99(0.03) | 8.12 | 0.28 | 0.76 | Red asymmetry | Orion |

**Notes.**
[a] $\delta V(12)\_13$ = (V12_peak-V12)/FWHM13.
[b] $\delta V(12)\_18$ = (V12_peak-V12)/FWHM18.

distribution. The decision to reject or accept the null hypothesis is based on comparing the $P$-value with the desired significance level, which is 0.05 in this paper. If the $P$-values from the K-S test are larger than 0.05, the parameter should follow the reference distribution. The statistics and K-S test results of the parameters are summarized in Table 7.

The distributions of $T_{12}$ and $T_{12}/T_{13}$ have a similar characteristic. Both have a power-law-like long tail, but cannot be described well with a lognormal distribution. The tail of the distribution of $T_{13}/T_{18}$ is less than those of $T_{12}$ and $T_{12}/T_{13}$, suggesting that $T_{12}$ may be a more sensitive physical element than $T_{13}$ and $T_{18}$ for star formation. The distribution of $T_{13}/T_{18}$ has a lognormal shape with a $P$-value for the K-S test as high as 0.234.

From Table 3 one can see that the line widths of the emission components are generally narrow. Most of the clumps have line widths smaller than 1.3 km s$^{-1}$. There are 162 high-mass clump candidates; among these, 68 have 2 or more velocity components. The clumps at high latitude all are low-mass clump candidates with a single component except for G159.23−34.49, which is in the high-mass group and has two components. Figure 4(a) presents the distributions of the FWHM of all three lines: the mean values and the standard deviations of the three line widths are 2.0 ± 1.3, 1.3 ± 0.8, and 0.8 ± 0.7 km s$^{-1}$, respectively. The shapes of all the distributions are similar to each other and are lognormally distributed.

### 3.3. Derived Physical Parameters

The excitation temperature derived from the radiation transfer equation is

$$T_r = \frac{T_a^*}{\eta_b} = \frac{h\nu}{k}\left[\frac{1}{\exp(h\nu/kT_{\rm ex})-1} - \frac{1}{\exp(h\nu/kT_{bg})-1}\right] \times [1-\exp(-\tau)]f. \quad (2)$$

Here, $T_r$ is the brightness temperature corrected with beam efficiency $\eta_b$. Assuming $^{12}$CO emission is optically thick ($\tau \gg 1$) and a filling factor of $f = 1$, the excitation temperature $T_{\rm ex}$ can be straightforwardly obtained. The $T_{\rm ex}$ is given in Column 6 of Table 4. We assume that the excitation temperatures of $^{13}$CO and C$^{18}$O are the same as that of the $^{12}$CO (1–0) in the following analysis. The values range from 3.9 K to 27 K, wider than the dust temperature range 7–17 K (Planck Collaboration et al. 2011a). The mean value with the standard deviation is 10 ± 2.6 K, which is smaller than the mean value of the dust temperature (12.8 ± 1.6 K) based on aperture photometry with

**Table 7**
A Statistical Analysis of Parameters

| Stat | $V_{12}-V_{13}$ (km s$^{-1}$) | $V_{13}-V_{18}$ (km s$^{-1}$) | $T_{12}$ (K) | $T_{12}/T_{13}$ | $T_{13}/T_{18}$ | FWHM(12) (km s$^{-1}$) | FWHM(13) (km s$^{-1}$) | FWHM(18) (km s$^{-1}$) | $N_{H_2}$ ($10^{21}$ cm$^{-2}$) | $T_{ex}$ (K) | $\tau(13)$ | $X_{13}/X_{18}$ | $\sigma_{NT}$ (km s$^{-1}$) | $\sigma_{Therm}$ (km s$^{-1}$) | $\sigma_{3D}$ (km s$^{-1}$) | $\sigma_{NT}/\sigma_{Therm}$ |
|---|---|---|---|---|---|---|---|---|---|---|---|---|---|---|---|---|
| | | | | | | | Statistics | | | | | | | | | |
| Number[a] | 782 | 437 | 904 | 782 | 437 | 904 | 782 | 437 | 782 | 782 | 782 | 437 | 782 | 782 | 782 | 782 |
| Mean | 0.02 | 0 | 3.08 | 2.15 | 3.88 | 2.03 | 1.27 | 0.76 | 4.4 | 10.1 | 0.93 | 7.0 | 0.53 | 0.17 | 0.98 | 3.09 |
| std | 0.29 | 0.16 | 1.37 | 1.35 | 1.71 | 1.28 | 0.77 | 0.73 | 3.6 | 2.6 | 0.56 | 3.8 | 0.31 | 0.02 | 0.51 | 1.83 |
| | Normal distribution fit | | Lognormal distribution fit | | | | | | | | | | | | | |
| $\mu$ | 0.02 | 0 | 1.02 | 0.65 | 1.26 | 0.56 | 0.10 | −0.44 | 1.22 | 2.29 | −0.24 | 1.83 | −0.77 | −1.76 | −0.12 | 0.99 |
| $\sigma$ | 0.29 | 0.16 | 0.48 | 0.43 | 0.45 | 0.55 | 0.51 | 0.53 | 0.78 | 0.24 | 0.62 | 0.46 | 0.51 | −0.12 | 0.43 | 0.53 |
| $P$ | 0 | 0 | 0 | 0 | 0.234 | 0.636 | 0.830 | 0.515 | 0 | 0.227 | 0 | 0.388 | 0.889 | 0.227 | 0.374 | 0.822 |

**Notes.** [a] Only the parameters of $^{13}$CO components are analyzed, but we also include those $^{12}$CO components without $^{13}$CO emission in statistics of $T_{12}$ and FWHM(12). Thirty-nine clumps without suitable reference positions in observations are excluded in statistics.

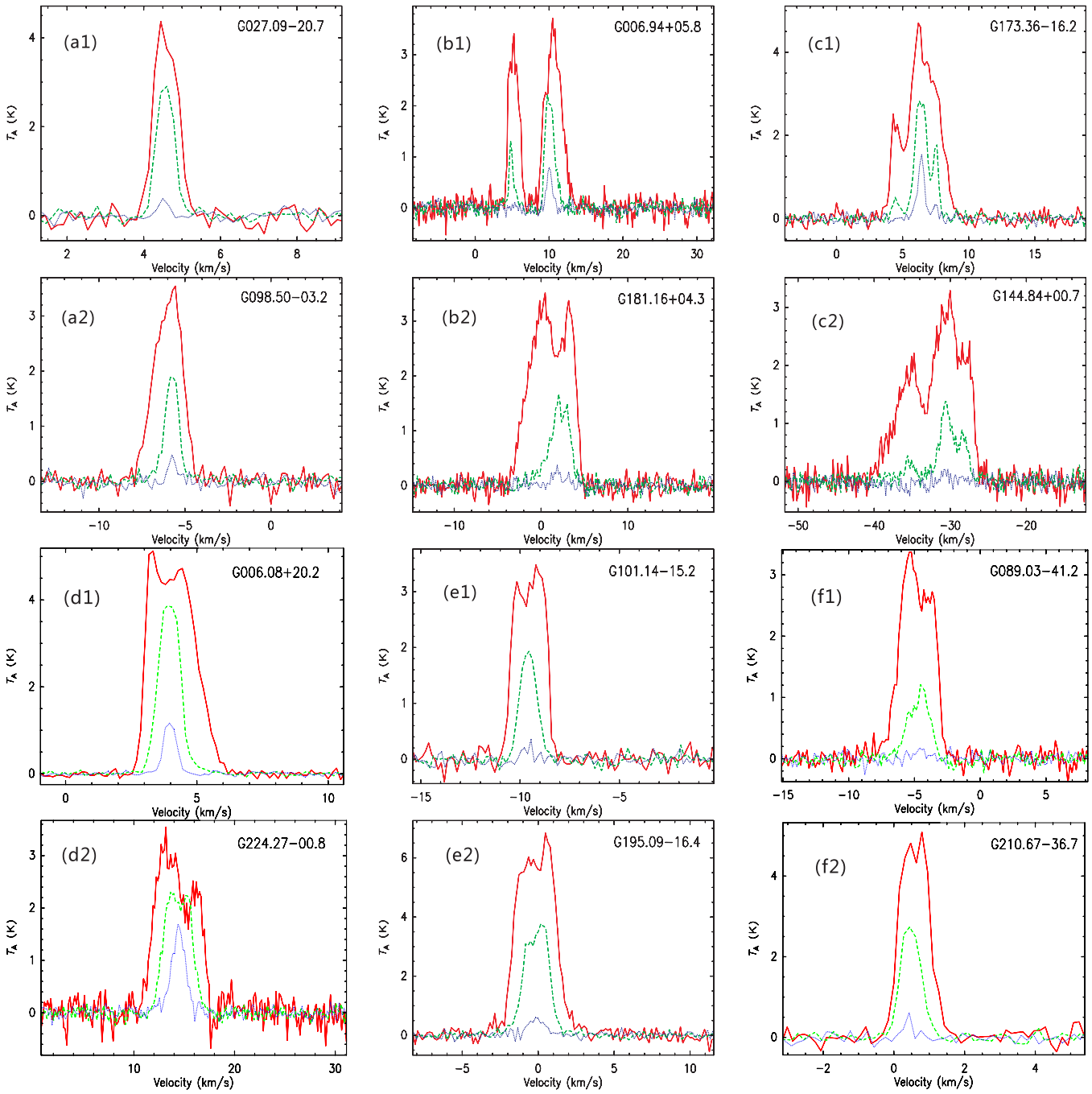


**Figure 1.** Examples of $J = 1$–0 lines of $^{12}$CO, $^{13}$CO, and C$^{18}$O spectra with different profiles. The classes are as follows: (a), (b), and (c) denote single, double, and triple velocity component spectra, respectively. (d) and (e) denote blue and red profiles; "1" and "2" denote low- and high-mass groups, respectively. (f1) and (f2) denote blue and red profiles of high-latitude clumps. (g), (h), and (i) denote blue asymmetry, red asymmetry, and the center dip, respectively; (j), (k), and (l) denote blue wings, red wings, and a pedestal, respectively; "1" and "2" denote the same as above.

(A color version of this figure is available in the online journal.)

a local background subtraction by *Herschel* photometric observations toward 71 Planck cold fields (Juvela et al. 2012), indicating the gas may be heated by the dust. There are 12 clumps with $T_{ex} > 17$ K. All of the hottest clumps are located in the Orion and Taurus regions, which suggests that high excitation temperature may be related to star formation conditions. Ninety-three components with $T_{ex} < 7$ K are referred to as coldest clumps among which G093.66+04.66 (3.9 K) is in the first quadrant, and G098.10+15.83 (5.0 K) and G112.63+20.80 (5.8 K) are in Cepheus. All other coldest clumps are the weaker components of the clumps with double or three emission components. The $T_{ex}$ histogram and its lognormal fit are shown in Figure 5. Its distribution can be well fitted by a lognormal shape with a $P$-value of the K-S test as large as 0.227, but the tail of the distribution seems to be much smaller than that of line widths and velocity dispersions. In the following analysis $T_{ex}$ was taken as the gas kinetic temperature assuming the local thermodynamic equilibrium (LTE) holds.

Both the optical depths $\tau_{13}$ and $\tau_{18}$ at the emission peak of the corresponding lines were calculated with

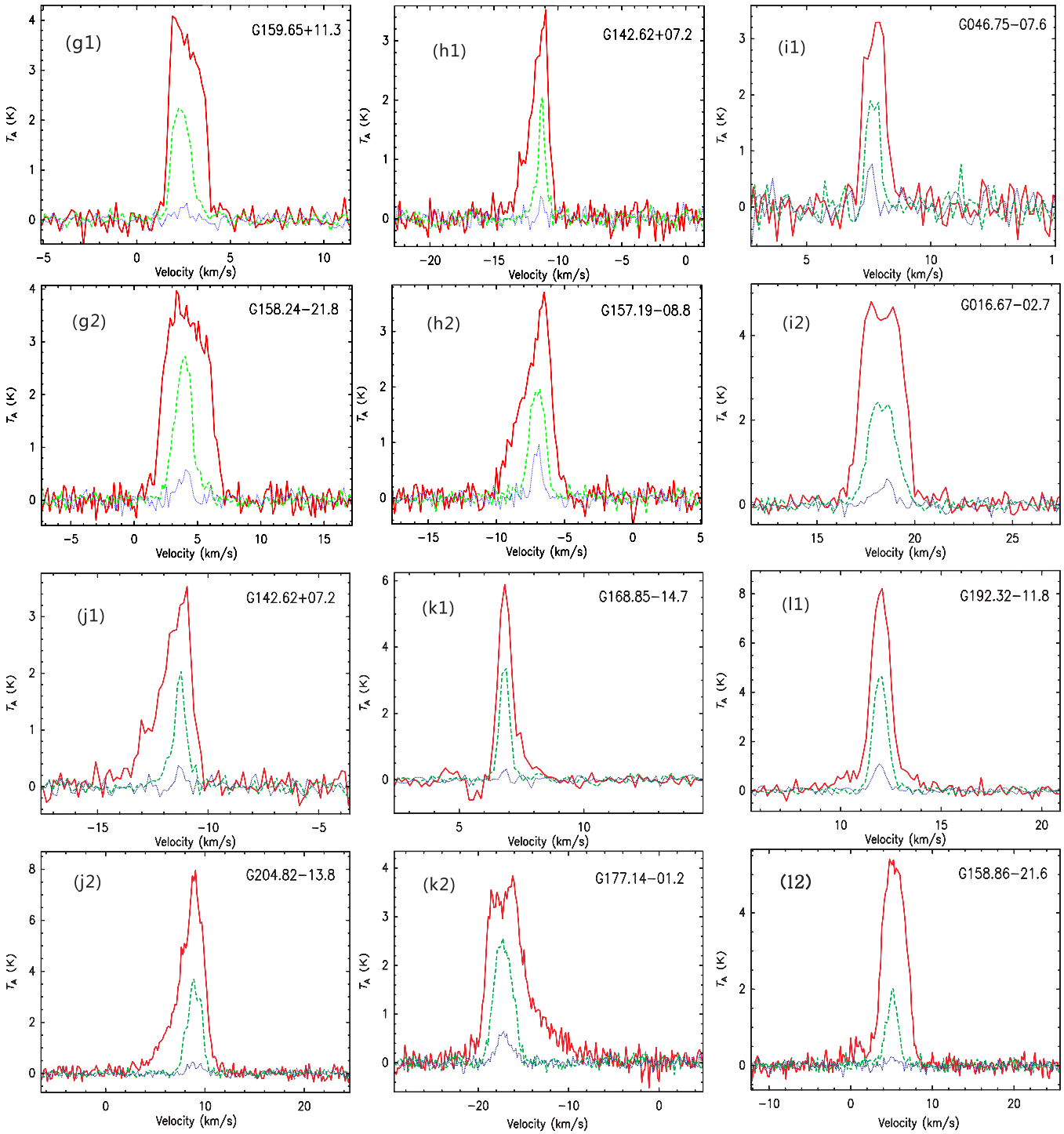


**Figure 1.** (Continued)

Equation (2) assuming the filling factor $f = 1$; these are listed in Columns 7 and 9 in Table 4. $\tau_{13}$ ranges from 0.1 to 4.1. The clumps with the largest $\tau_{13}$ include G026.45−08.02 (3.2) and G058.07+03.29 (3.2) of the first quadrant, G164.94−08.57 (4.1) and G179.10−06.27 (3.9) in Taurus, and G182.04+00.41 (3.8) located at anticenter. For the 10 clumps with the smallest optical depth (0.1), all of them are the minor components of the multiple-component sources except for G121.88−08.76. Figure 6(a) shows the histogram of $\tau_{13}$ and its lognormal fitting. The mean value is $0.93 \pm 0.56$.

The column density of a molecular line can be obtained with the theory of radiation transfer and molecular excitation as follows (Garden et al. 1991):

$$N = \frac{3k}{8\pi^3 B\mu^2} \frac{\exp[hBJ(J+1)/kT_{\rm ex}]}{(J+1)} \times \frac{(T_{\rm ex} + hB/3k)}{[1-\exp(-h\nu/kT_{\rm ex})]} \int \tau_V dV, \quad (3)$$

where $B$, $\mu$, and $J$ are the rotational constant, the permanent dipole moment, and the rotational quantum number of the

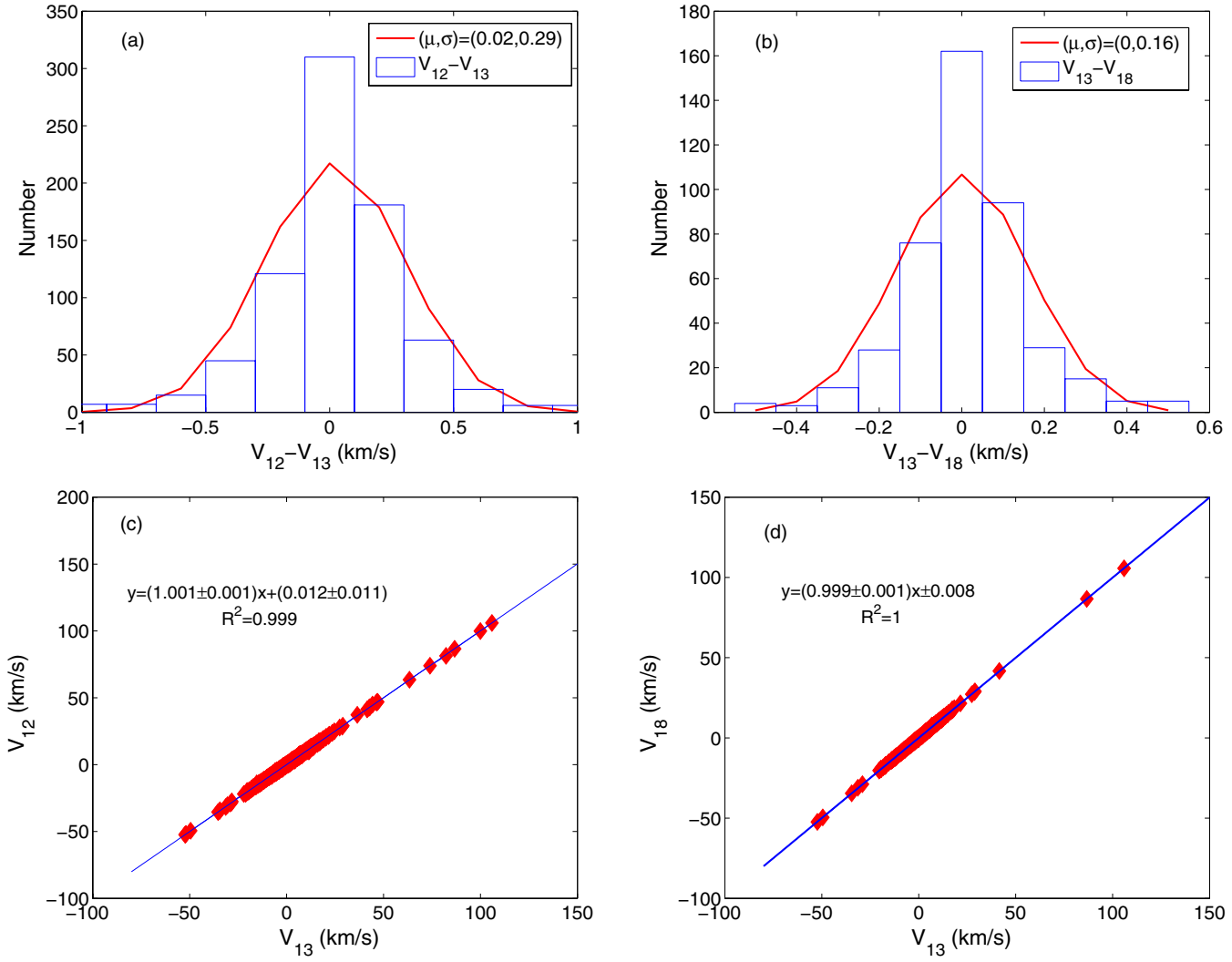


**Figure 2.** Line center velocities of the $J = 1$–0 lines of $^{12}$CO, $^{13}$CO, and C$^{18}$O. (a) and (b) are the histogram and the normal distribution fits for the difference between $V_{12}$ and $V_{13}$, $V_{13}$ and $V_{18}$, respectively. The mean $\mu$ and standard deviation $\sigma$ of the normal distributions are presented in the upper-right boxes; (c) and (d) plot for $V_{12}$ vs. $V_{13}$ and $V_{13}$ vs. $V_{18}$, respectively.

(A color version of this figure is available in the online journal.)

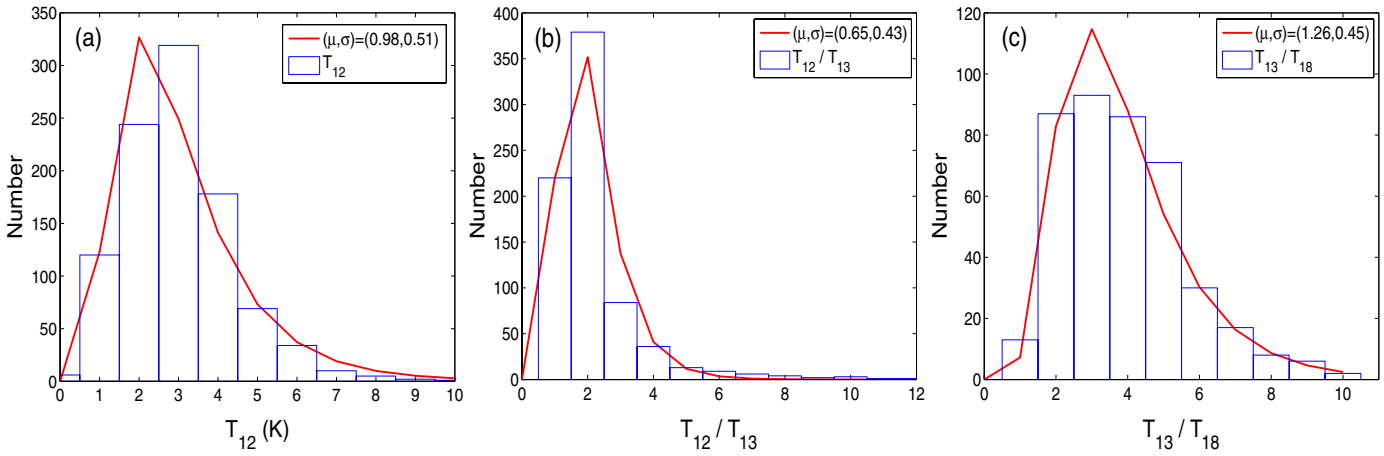


**Figure 3.** Frequency distributions of the antenna temperature $T_{12}$, the ratio of $T_{12}/T_{13}$, and $T_{13}/T_{18}$.

(A color version of this figure is available in the online journal.)

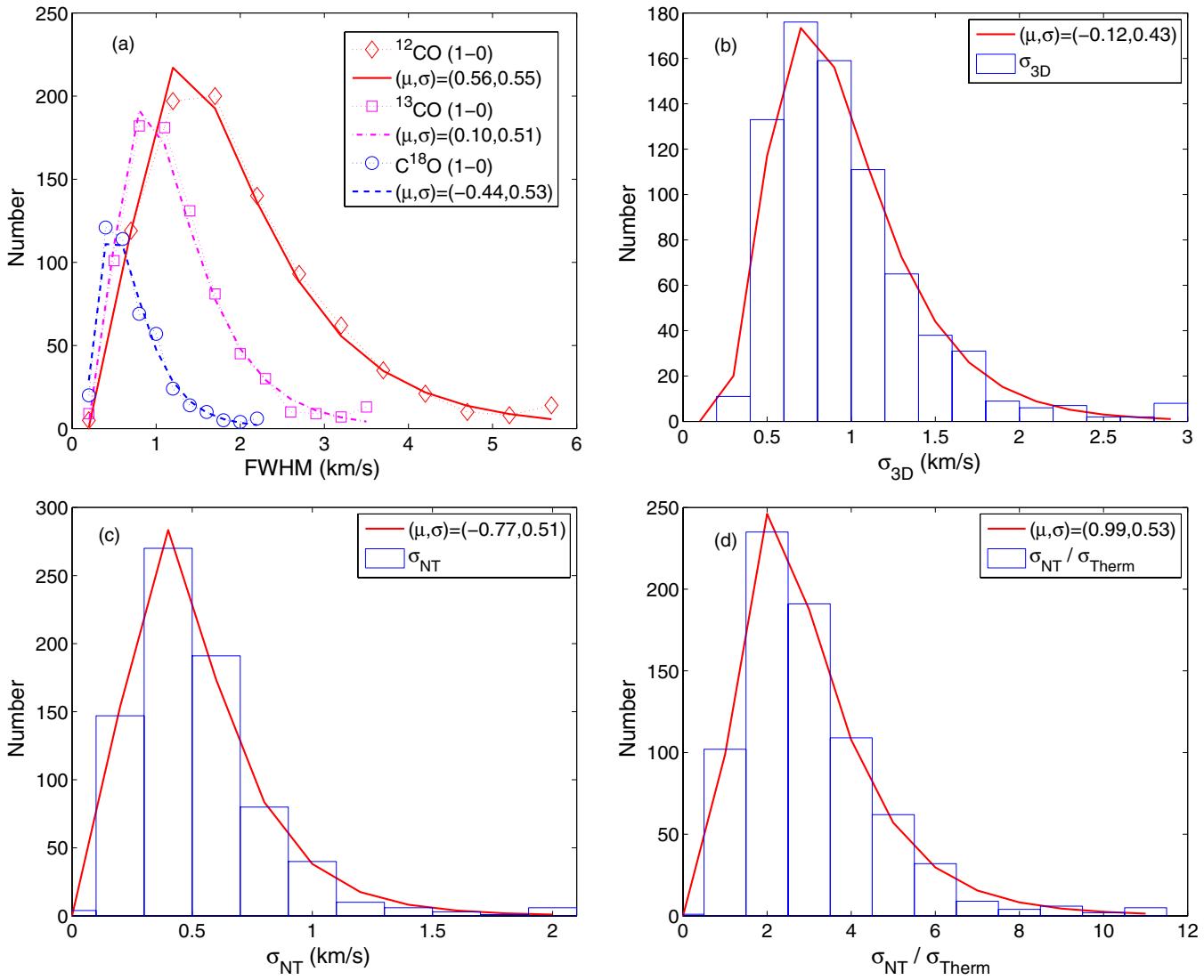


**Figure 4.** Frequency distributions of the line FWHMs and velocity dispersions. (a) Distributions and lognormal fitting of the FWHMs of the CO, $^{13}$CO, and C$^{18}$O lines. (b) Histogram and the lognormal fitting of the $^{13}$CO line 3D velocity dispersion. (c) Velocity dispersion of nonthermal motion $^{13}$CO lines. (d) Histogram and lognormal fitting of the ratio of the $^{13}$CO line nonthermal and thermal motion. The mean $\mu$ and standard deviation $\sigma$ of the lognormal distribution fits are presented in the upper-right boxes in each panel.

(A color version of this figure is available in the online journal.)

lower state of the molecular transition. Column densities of the $^{13}$CO and C$^{18}$O molecules were calculated and given in Columns 8 and 10 of Table 4. The maximum C$^{18}$O column densities of the Planck clumps are $1.1 \times 10^{16}$ cm$^{-2}$ and $1.3 \times 10^{15}$ cm$^{-2}$ in G028.56−00.24 and G160.51−16.84, respectively, and the smallest ones are $1.0 \times 10^{14}$ cm$^{-2}$ in G26.93−20.68 and G102.72−25.96. The column densities of the C$^{18}$O span a wider range than those of the nearby dark clouds (Myers et al. 1983) which are from $3 \times 10^{14}$ to $2.7 \times 10^{15}$ cm$^{-2}$. The different column density ranges between our sample and the nearby dark clouds may be attributed to the larger space distribution of Planck cold clumps than the nearby dark clouds.

The $^{13}$CO column densities were calculated for 782 velocity components. For the 437 components with both C$^{18}$O and $^{13}$CO column densities, the abundance ratio of $X_{13}/X_{18}$ was calculated and listed in Column 13 of Table 4. The histogram and the lognormal distribution of $X_{13}/X_{18}$ fitting are presented in Figure 6(b). The distribution shape of the ratio $X_{13}/X_{18}$ is similar to that of $\tau_{13}$. The mean value of $X_{13}/X_{18}$ is 7.0 ± 3.8, higher than that of the terrestrial ratio 5.5. The distribution of $X_{13}/X_{18}$ can be well depicted by a lognormal distribution with a *P*-value of the K-S test as high as 0.388.

Molecular hydrogen column densities of each velocity component were derived according to the column densities of the $^{13}$CO. The fractional abundance of $[H_2]/[^{13}CO] = 89 \times 10^4$ was adopted. We also calculated the $N_{H_2}$ for the components without $^{13}$CO emission by assuming $^{12}$CO (1–0) emission to be optically thin, the excitation temperature of 10 K and $[H_2]/[^{12}CO] = 10^4$, but these components are excluded in further statistics. Figure 6(c) presents the plots of the $N_{H_2}$ histogram and its lognormal fitting. It spans from $10^{20}$ to $4.5 \times 10^{22}$ cm$^{-2}$, which is larger than that of the eight sources on average (Planck Collaboration et al. 2011b). From *Herschel* follow-up observations, the peak column densities of 71 clumps range from $4 \times 10^{20}$ to $7.4 \times 10^{22}$ (Juvela et al. 2012), which are slightly larger than the column densities obtained in this work. The four clumps

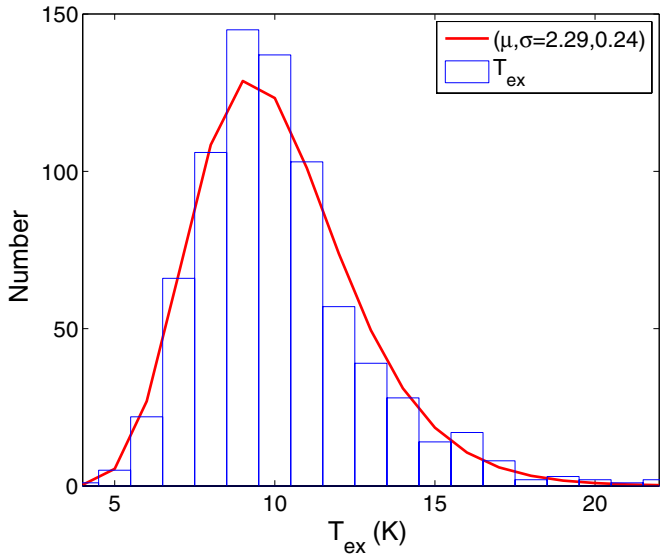


**Figure 5.** Histogram and the lognormal-PDF fitting of excitation temperatures. (A color version of this figure is available in the online journal.)

with the largest $^{13}$CO column densities are G209.28−19.62, G028.56−00.24, G033.70−00.01, and G158.37−20.72. The $N_{H_2}$ of G209.28−19.62 located in the Orion complex is as high as $4.5 \times 10^{22}$ cm$^{-2}$. G028.56−00.24 and G033.70−00.01, with $N_{H_2}$ of 3.4 and 2.8 $\times$ $10^{22}$ cm$^{-2}$, are located in the first quadrant. G158.37−20.72, with $N_{H_2}$ of $2.3 \times 10^{22}$ cm$^{-2}$, is in Taurus, which is 7′ north of NGC 1333 (Strom et al. 1976) and has a very red young star, SSV 13 (Harvey et al. 1998). The $^{12}$CO lines of all these clumps have large line widths of 2.57–9.35 km s$^{-1}$, showing turbulence support for these clumps. The column density distribution (Figure 6(c)) cannot be fitted with a unique lognormal distribution, but exhibits a power-law-like tail, similar to that identified from active star formation regions (Kainulainen et al. 2009), indicating that some Planck cold clumps are located in active star-forming regions.

The one-dimensional nonthermal ($\sigma_{NT}$) and thermal ($\sigma_{Therm}$) velocity dispersions can be estimated as follows:

$$\sigma_{NT} = \left[\sigma^2_{^{13}CO} - \frac{kT_{ex}}{m_{^{13}CO}}\right]^{\frac{1}{2}} \quad (4)$$

$$\sigma_{Therm} = \left[\frac{kT_{ex}}{m_H \mu}\right]^{\frac{1}{2}}, \quad (5)$$

where $\sigma_{^{13}CO} = (\Delta V_{13}/8\ln(2))$ and $T_{ex}$ are the one-dimensional velocity dispersion of the $^{13}$CO (1–0) and excitation temperature, respectively. $k$ is the Boltzmann's constant, $m_{^{13}CO}$ is the mass of $^{13}$CO, $m_H$ is the mass of atomic hydrogen, and $\mu = 2.72$ is the mean molecular weight of the gas. Then the 3D velocity dispersion $\sigma_{3D}$ can be estimated as

$$\sigma_{3D} = \left(3\left(\sigma^2_{Therm} + \sigma^2_{NT}\right)\right)^{1/2}. \quad (6)$$

The 3D and nonthermal velocity dispersions shown in Figures 4(b) and (c) also present a similar distribution as line widths. As shown in Table 7, the $P$-values of the K-S test for a lognormal hypothesis for line widths and velocity dispersions are all much larger than 0.05, indicating that their distributions can be remarkably well described by a lognormal fit. The lognormal behaviors of volume or column density in molecular clouds were frequently reported in recent observations (Ridge et al. 2006; Froebrich et al. 2007; Goodman et al. 2009), which are often interpreted as a consequence of supersonic turbulence in the observed clouds (Vázquez-Semadeni 1994). From our results, the effect of supersonic turbulence in the clouds should be more likely reflected in the lognormal behaviors of the distributions of line widths and velocity dispersions than in the distributions of column density. Figure 4(d) plots the distribution for the ratios of $\sigma_{NT}$ to $\sigma_{Therm}$. One can see that most of the clumps have $\sigma_{NT}$ larger than $\sigma_{Therm}$, indicating that turbulent motions dominate in these clouds. The shape of their ratio distribution is similar to the distributions of the FWHM of the three transitions, the $\sigma_{3D}$ and $\sigma_{NT}$, but the tail part is narrower than the others, which may suggest that the thermal motions may not be as sensitive as nonthermal motions for revealing star formation activity.

### 3.4. Mapping Results

In the 10 mapped clumps, 12 velocity components were detected. Six of them have FWHMs of $^{13}$CO (1–0) larger than 1.3 km s$^{-1}$ and the other four belong to group L. The CO line profiles of the clump G089.64−06.59, one of the velocity components of G157.60−12.17, G179.29+04.20, and G196.21−15.50, show a blue asymmetric signature. The integrated intensities are shown in the contour maps in Figure 7. The morphologies of these clumps are different. G001.38+20.94 and G180.92+04.53 show both diffuse features and a dense clump. G108.85−00.80, G157.60−12.17b, and G196.21−15.50 exhibit a filamentary shape with a chain of dense clumps. G161.43−35.59 and G194.80−03.41 also appear as a dumbbell in filamentary structure. Four cores are detected in G006.96+00.89a and G161.43−35.59, respectively. G049.06−04.18 is an isolate clump while G089.64−06.59 shows a cometary-like structure. Filamentary structures are the majority among these clumps, which is consistent with the *Herschel* follow-up observation results (Juvela et al. 2012). Juvela et al. (2012) also found that the filaments often fragment into substructures. Such behavior is revealed in the gas emission too as in G006.96+00.89a shown in Figure 7.

There are 22 cores identified with two-dimensional Gaussian fits to the 10 mapped sources. The physical parameters of these cores are presented in Table 8. The positions of the cores are shown as offset relative to the reference positions in Column 4. Deconvolved sizes $a$ and $b$ (Column 5) are the major and minor angular sizes of the cores and measured from the contours at half of the maximum intensity of the $^{13}$CO (1–0) lines. The radius $R = ((ab)^{1/2}/2)D$, where $D$ is the distance, in Column 6 distributes from several tenths to about 3 of kpc. Columns 7–12 list the clump parameters: $T_{ex}$, $N_{H_2}$, velocity dispersions, and volume density $n_{H_2} = N_{H_2}/2R$, respectively. Then the core mass can be derived as $M = (4/3)\pi \cdot R^3 \cdot n_{H_2} \cdot m_{H_2} \cdot \mu_g$, where $m_{H_2}$ is the mass of a hydrogen molecule and $\mu_g = 1.36$ is the mean atomic weight of the gas. Core mass calculated with LTE assumption is given in Column 13. Columns 14 and 15 are the virial mass and the Jeans mass, respectively (see the next section). The final three columns are the morphology, the group, and the location of the clumps. The column density of the cores ranges from 1.3 to 7.7 $\times$ $10^{21}$ cm$^{-2}$. The LTE masses of the cores range from 9 to $1.5 \times 10^4$ $M_\odot$ with a median value of 110 $M_\odot$. In the *Herschel* follow-up observations, the 26 identified filaments have column densities ranging from 0.9 to 19.2 $\times$ $10^{21}$ cm$^{-2}$ and masses ranging from 3.2 $\times$ $10^3$ with a median value of

**Table 8**
Parameters of the 10 Mapped Clumps

| Name | $V_{lsr}$ (km s$^{-1}$) | $d$ (kpc) | Offset ($''$, $''$) | Deconvolved Size ($'' \times ''(^\circ)$) | $R$ (pc) | $T_{ex}$ (K) | $N_{H_2}$ ($10^{21}$ cm$^{-2}$) | $\sigma_{Therm}$ (km s$^{-1}$) | $\sigma_{NT}$ (km s$^{-1}$) | $\sigma_{3D}$ (km s$^{-1}$) | $n$ ($10^3$ cm$^{-3}$) | $M_{LTE}$ ($M_\odot$) | $M_{vir}$ ($M_\odot$) | $M_J$ ($M_\odot$) | Group | Region |
|---|---|---|---|---|---|---|---|---|---|---|---|---|---|---|---|---|
| G001.38+20.94 | 0.74 | 1.1 | (−110,−41) | 677 × 428(67.9) | 1.4 | 14.1(0.9) | 5.3(1.7) | 0.21(0.01) | 0.33(0.09) | 0.67(0.13) | 0.6 | 751 | 150 | 43 | L | Ophiuchus |
| G006.96+00.89a_1 | 9.33 | 2.21 | (5,−91) | 187 × 119(−8.1) | 0.8 | 9.9(0.4) | 3.2(0.7) | 0.17(0.00) | 0.88(0.19) | 1.56(0.32) | 0.6 | 141 | 453 | 496 | H | Fourth quad |
| G006.96+00.89a_2 | 9.33 | 2.21 | (−90,30) | 149 × 102(−42.5) | 0.7 | 9.7(0.5) | 2.6(0.9) | 0.17(0.00) | 0.70(0.20) | 1.25(0.34) | 0.6 | 78 | 240 | 260 | | Fourth quad |
| G006.96+00.89a_3 | 9.33 | 2.21 | (−207,39) | 301 × 64(−70.9) | 0.7 | 9.4(0.3) | 3.2(1.0) | 0.17(0.00) | 0.92(0.01) | 1.61(0.17) | 0.7 | 122 | 449 | 544 | | Fourth quad |
| G006.96+00.89a_4 | 9.33 | 2.21 | (−334,66) | 268 × 143(89.1) | 1.0 | 8.9(0.7) | 2.7(0.7) | 0.16(0.01) | 1.02(0.30) | 1.79(0.51) | 0.4 | 204 | 783 | 945 | | Fourth quad |
| G006.96+00.89b | 41.67 | 5.36 | (−64,−1) | 203 × 161(38.2) | 2.3 | 10.7(1.1) | 6.8(2.6) | 0.18(0.01) | 1.52(0.22) | 2.66(0.37) | 0.5 | 2579 | 3873 | 2905 | H | Fourth quad |
| G049.06−04.18 | 9.93 | 0.6 | (16,41) | 239 × 194(−51.9) | 0.3 | 8.9(1.2) | 1.3(0.5) | 0.16(0.01) | 0.15(0.04) | 0.39(0.05) | 0.7 | 9 | 11 | 7 | L | First quad |
| G089.64−06.59 | 12.51 | 0.6 | (81,−20) | 320 × 187(−0.9) | 0.4 | 10.2(0.9) | 3.4(1.5) | 0.18(0.01) | 0.40(0.09) | 0.74(0.15) | 1.5 | 30 | 45 | 38 | L | First quad |
| G108.85−00.80 | −49.51 | 5.4 | (−20,−12) | 776 × 213(45.1) | 5.3 | 11.5(3.7) | 7.7(5.4) | 0.18(0.03) | 0.89(0.28) | 1.58(0.46) | 0.2 | 14993 | 3096 | 858 | H | Second quad |
| G157.60−12.17a | −7.75 | 1.17 | (−38,−44) | 432 × 283(16.4) | 1.0 | 10.4(0.9) | 3.6(1.2) | 0.18(0.01) | 0.40(0.01) | 0.76(0.12) | 0.6 | 243 | 133 | 61 | L | Taurus |
| G157.60−12.17b_1 | −2.58 | 0.47 | (−83,−63) | 535 × 421(41.7) | 0.5 | 14.7(1.6) | 4.1(1.5) | 0.21(0.01) | 0.43(0.11) | 0.83(0.17) | 1.2 | 82 | 87 | 55 | L | Taurus |
| G157.60−12.17b_2 | −2.58 | 0.47 | (−197,−278) | 301 × 196(52.2) | 0.3 | 14.6(1.3) | 4.1(1.4) | 0.21(0.01) | 0.60(0.13) | 1.11(0.21) | 2.4 | 22 | 79 | 92 | | Taurus |
| G161.43−35.59_1 | −5.83 | 1.49 | (60,212) | 269 × 143(−12.5) | 0.7 | 9.8(0.4) | 2.3(0.5) | 0.17(0.00) | 0.29(0.06) | 0.59(0.09) | 0.5 | 79 | 57 | 29 | L | High Glat |
| G161.43−35.59_2 | −5.83 | 1.49 | (−3,−49) | 261 × 150(82) | 0.7 | 12.0(1.2) | 2.6(0.8) | 0.19(0.01) | 0.18(0.03) | 0.46(0.04) | 0.6 | 91 | 35 | 13 | | High Glat |
| G161.43−35.59_3 | −5.83 | 1.49 | (−166,−71) | 387 × 168(87.6) | 0.9 | 10.5(0.9) | 2.2(0.5) | 0.18(0.01) | 0.20(0.03) | 0.47(0.04) | 0.4 | 128 | 47 | 17 | | High Glat |
| G161.43−35.59_4 | −5.83 | 1.49 | (−303,−86) | 141 × 140(−21.1) | 0.5 | 10.7(0.9) | 1.9(0.6) | 0.18(0.01) | 0.25(0.06) | 0.53(0.09) | 0.6 | 34 | 33 | 21 | | High Glat |
| G180.92+04.53 | 0.98 | 3.62 | (0,−12) | 359 × 339(62.2) | 3.1 | 9.1(0.6) | 3.4(1.1) | 0.17(0.01) | 0.59(0.11) | 1.07(0.19) | 0.2 | 2191 | 817 | 303 | H | Third quad |
| G194.80−03.41_1 | 12.84 | 2.89 | (−4,−19) | 690 × 341(81.3) | 3.4 | 9.8(0.5) | 4.5(1.7) | 0.18(0.01) | 0.86(0.31) | 1.52(0.52) | 0.2 | 3573 | 1829 | 812 | H | Third quad |
| G194.80−03.41_2 | 12.84 | 2.89 | (−132,331) | 355 × 242(61.3) | 2.1 | 10.3(0.9) | 5.3(2.4) | 0.17(0.01) | 0.78(0.20) | 1.28(0.34) | 0.4 | 1536 | 784 | 436 | | Third quad |
| G196.21−15.50_1 | 3.76 | 0.8 | (−79,5) | 276 × 203(54.2) | 0.5 | 14.5(0.8) | 3.1(0.9) | 0.21(0.01) | 0.32(0.12) | 0.68(0.16) | 1.1 | 45 | 49 | 30 | H | Orion |
| G196.21−15.50_2 | 3.76 | 0.8 | (104,126) | 228 × 84(3.5) | 0.3 | 15.1(0.8) | 2.8(0.7) | 0.21(0.01) | 0.31(0.07) | 0.65(0.11) | 1.7 | 14 | 26 | 22 | | Orion |
| G196.21−15.50_3 | 3.76 | 0.8 | (265,85) | 256 × 89(60.8) | 0.3 | 14.6(0.6) | 2.5(0.9) | 0.21(0.00) | 0.30(0.12) | 0.66(0.15) | 1.4 | 15 | 30 | 23 | | Orion |

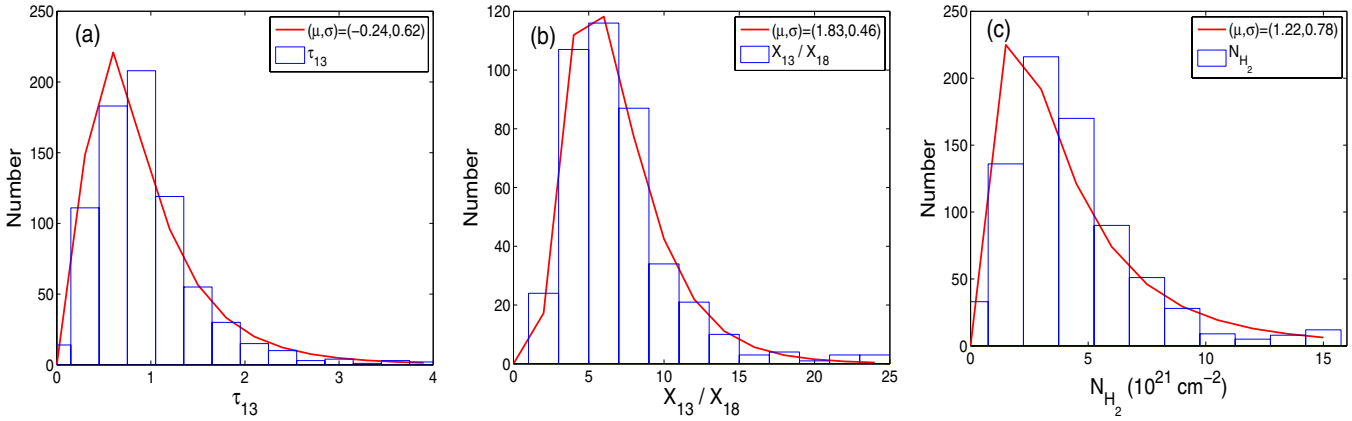


**Figure 6.** Histograms of $\tau_{13}$, ratio [X_13/X_18], and column density $N_{H_2}$, and their lognormal-PDF fitting.
(A color version of this figure is available in the online journal.)

120 $M_\odot$ (Juvela et al. 2012), which are consistent with the case of the cores in this work.

## 4. DISCUSSION

### 4.1. Line Center Velocities

The coincidence of three transitions observed toward the Planck clumps is not usual in star formation regions. Line center velocities of different molecular species could be significantly offset from the systematic velocity in active star-forming regions. In the six $NH_3$ clumps of G084.81−01.09, the deviations between the $^{12}$CO and $^{13}$CO are all larger than 1 km s$^{-1}$ (Zhang et al. 2011). $V_{\rm lsr}$ of the $^{12}$CO deviated from that of $^{13}$CO or C$^{18}$O are also seen in IRDCs. In 61 IRDCs, there are 10% of sources with $V_{\rm lsr}$ deviation of $\gtrsim$ 1 km s$^{-1}$ from the $^{12}$CO and the C$^{18}$O lines (Du & Yang 2008). The rather large discrepancy between the $V_{\rm lsr}$ of $^{12}$CO and $^{13}$CO can also be seen in the submillimeter clumps (Qin et al. 2008). The line center velocity difference of various molecular species may originate from molecular layers with different temperatures or trace different kinematical gas layers (Bergin et al. 1997; Muller et al. 2011). The deviation between $V_{13}$ and $V_{18}$ of the Planck clumps also tends to be smaller than those of Myers et al. (1983). All of these suggest that the cold clumps are the quietest molecular regions found so far as a whole.

### 4.2. Distances of the Clumps

Distance is essential for investigating the spatial distribution and physical conditions of the clumps. The Planck Collaboration et al. (2011d) have estimated the distance for 2619 C3PO clumps using various extinction signatures. They also found that there are 127 Planck cold clumps associated with IRDCs which have a kinematic distance from Simon et al. (2006). In our sample there are only two clumps close to the sources of Simon et al. (2006) at the zero latitude Galactic layer. There is certainly a part of the ECC clumps with distance estimated using extinction methods. We estimated the kinematic distances of the clumps using the $V_{\rm lsr}$ of the clumps which could be a comparison for those with known distance. We adopt the rotation curve of Clemens (1985) $R_\odot = 8.5$ kpc and $\Theta_\odot = 220$ km s$^{-1}$ in our calculation. To see the possible physical relation of the components in clumps with double and triple peaks, the distance of each component was calculated. For the clumps within the inside of the solar circle there are two solutions. The clumps are perhaps located at the front of the Galactic bulk of the diffuse background, since extinction is rising along a line of sight that crosses a dust clump (Planck Collaboration et al. 2011a). For this reason, the near value of the distances was adopted. Among our sample there are a number of clumps that are located in molecular complexes with known distances. Since these complexes have rather large areas and clumps residing inside them have different $V_{\rm lsr}$, the kinematic distances of the clumps within one complex are quite different as well. Therefore, for every clump within the same complex, their distances are also given as the kinematic distances. However, in a case where there is some ambiguity about the distance of the clump, the one close to the known distance of the complex was adopted.

The histogram of the kinematic distances is plotted in Figure 8. Distances were obtained for 741 $^{13}$CO components. Of the components, 51% have distances within 0.5 and 1.5 kpc. The mean value is 1.57 kpc, lower than those associated with IRDCs by Simon et al. (2006). The reason for this may be due to cloud properties; most of our clumps or components belong to the low-mass group and the IRDCs of Simon et al. (2006) are at the fourth quadrant of the mid-plane and with distances between 0.4 and 7.8 kpc (Simon et al. 2006).

### 4.3. Physical Parameter Distributions in the Galaxy

#### 4.3.1. Excitation Temperature and the Ratio of Line Strengths of $^{12}$CO and $^{13}$CO

Figure 9 presents the distribution of the $T_{\rm ex}$ and the ratio of $T_{12}/T_{13}$. Figures 9(a) and (c) are for radial changes and (b) and (d) are for the altitude from the Galactic plane. The excitation temperature is higher than 10 K from 4 to 8 kpc. Early observations also showed the high excitation of the gas emission at the 3–7 kpc molecular ring (Scoville & Sanders 1987). Around 8 kpc, $T_{\rm ex}$ is also larger than 10 K, which may be related to the emission of the giant molecular clouds near the Sagittarius arm. The ratio of $T_{12}$ to $T_{13}$ is high at $R \sim 5$ kpc, then deceases with $R$ and has a valley between 5 and 8 kpc, then a lowest value at ∼6 kpc, suggesting that the brightness temperature of $^{13}$CO (1–0) is relatively high in this region.

Figure 9(b) shows that excitation temperature changes with the altitude. There are two peaks 11 and 13 K at $Z \sim 350$ pc and ∼470 pc, respectively. The changes of the ratio of $T_{12}/T_{13}$ shown in Figure 9(d) are rather smooth and reach a low value at $Z \sim 470$ pc, suggesting the brightness temperature of $^{13}$CO is relatively high at this altitude.

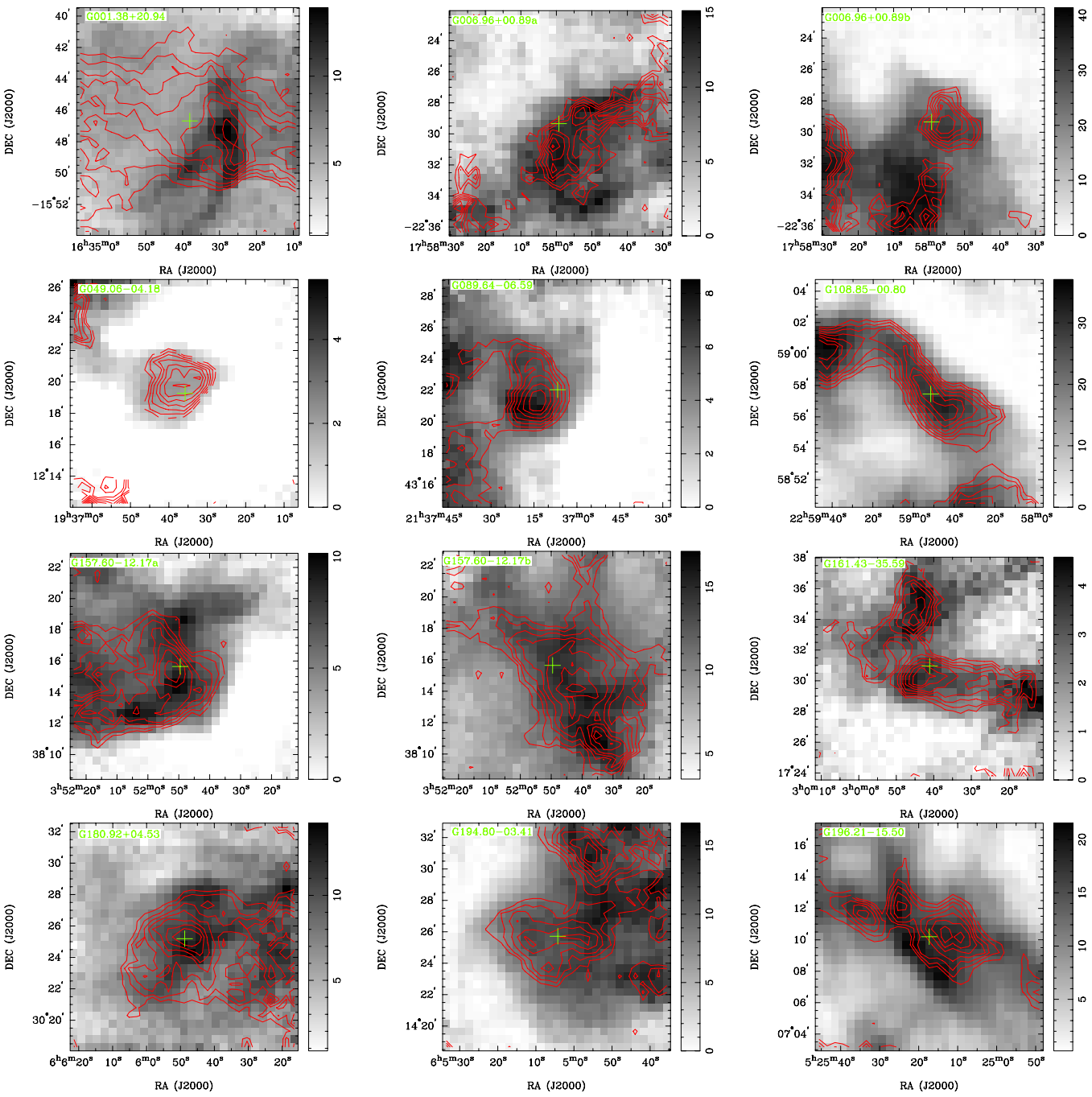


**Figure 7.** Integration intensity images of the mapped clumps: contours for the $^{13}$CO line and the gray scale for the $^{12}$CO lines. The contours are from 30% to 90% in a step of 10% of the peak value.

(A color version of this figure is available in the online journal.)

#### 4.3.2. Velocity Dispersion

Variations of the velocity dispersion with the distance from the Galactic center and the altitude from the Galactic plane are investigated. The radial variations of $\sigma_{3D}$, $\sigma_{NT}$, and the ratio of $\sigma_{NT}/\sigma_{Therm}$ are plotted in Figures 10(a), (c), and (e), respectively. The variation of the $\sigma_{3D}$ and $\sigma_{NT}$ as well as the ratio of $\sigma_{NT}/\sigma_{Therm}$ with $R$ are about the same and they reached the maximum at $R \sim 5$ kpc, which suggests that the dynamic process is most violent at the 5 kpc Galactic ring. From 6 kpc, the $\sigma_{3D}$, $\sigma_{NT}$, and the ratio of $\sigma_{NT}/\sigma_{Therm}$ seem to linearly increase with $R$, indicating that turbulence becomes more violent in the outer part of the Galaxy.

Figures 10(b), (d), and (f) present changes of the velocity dispersions $\sigma_{3D}$, $\sigma_{NT}$, and the ratio of $\sigma_{NT}/\sigma_{Therm}$ with the altitude. One can see that they all decrease with increasing altitude from the Galactic disk to heights of 475–525 pc, showing that the turbulent process is stronger closer to the Galactic plane. At $Z \sim 680$ pc all of them reached a minor peak. We found the clumps at this minor peak are distributed around ($l \sim 174°, b \sim 17°$) or ($l \sim 4°, b \sim -17°$); this minor peak may be concerned with the emission regions of Taurus and $\rho$ Oph. From panels (e) and (f), one can see that nonthermal motion dominates the line broadening. This is the first time evidence for nonthermal line broadening has been obtained from a survey of the $^{13}$CO (1–0) lines.

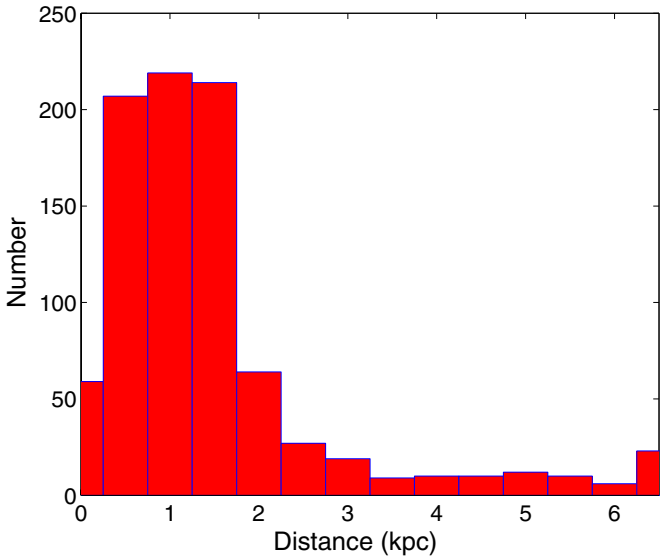


**Figure 8.** Frequency distribution of the kinematic distances.
(A color version of this figure is available in the online journal.)

One can see that there are some differences among the radial variations of the velocity dispersion and excitation temperature. The maximum of $T_{ex}$–$R$ variation is at rather high values around 4–8 kpc and reaches maximum at 6 kpc. The $T_{ex}$ variation is milder than that of $\sigma_{NT}$ suggesting that the gas heating and cooling occur in a wider spatial region than the turbulence.

#### 4.3.3. $^{13}CO$ Opacity, $X_{13}/X_{18}$, and $H_2$ Column Density

Figure 11(a) shows the radial variation of the optical depth of the $^{13}CO$ (1–0) lines. The smallest value is at the 5 kpc ring. Between 5.5 and 8 kpc there is a high feature, then it decreases until 14 kpc. One reason for the low valley is that $T_{ex}$ is rather high around 5 kpc (see Figure 9(a)). Besides, its emission is relatively low compared with that of $^{12}CO$. For example, G017.22−01.47 at $R = 4.90$ kpc is $\tau_{13} = 0.3$, $T_{ex} = 10.1$ K, and $T_{13} = 0.88$ K; G033.70−00.01, $R = 5.05$ kpc, $\tau_{13} = 0.5$, $T_{ex} = 9.2$ K, and $T_{13} = 1.12$ K; and G028.56−00.24, $R = 4.96$ kpc, $\tau_{13} = 0.3$, $T_{ex} = 10.1$ K, and $T_{13} = 0.92$ K.

The ratio of $X_{13}$ to $X_{18}$ presented in Figure 11(c) is rather low, between 5 and 7 kpc, and its corresponding values range from ∼6 to 7, still higher than the terrestrial value. At 8 kpc and >10 kpc the value is near 8.

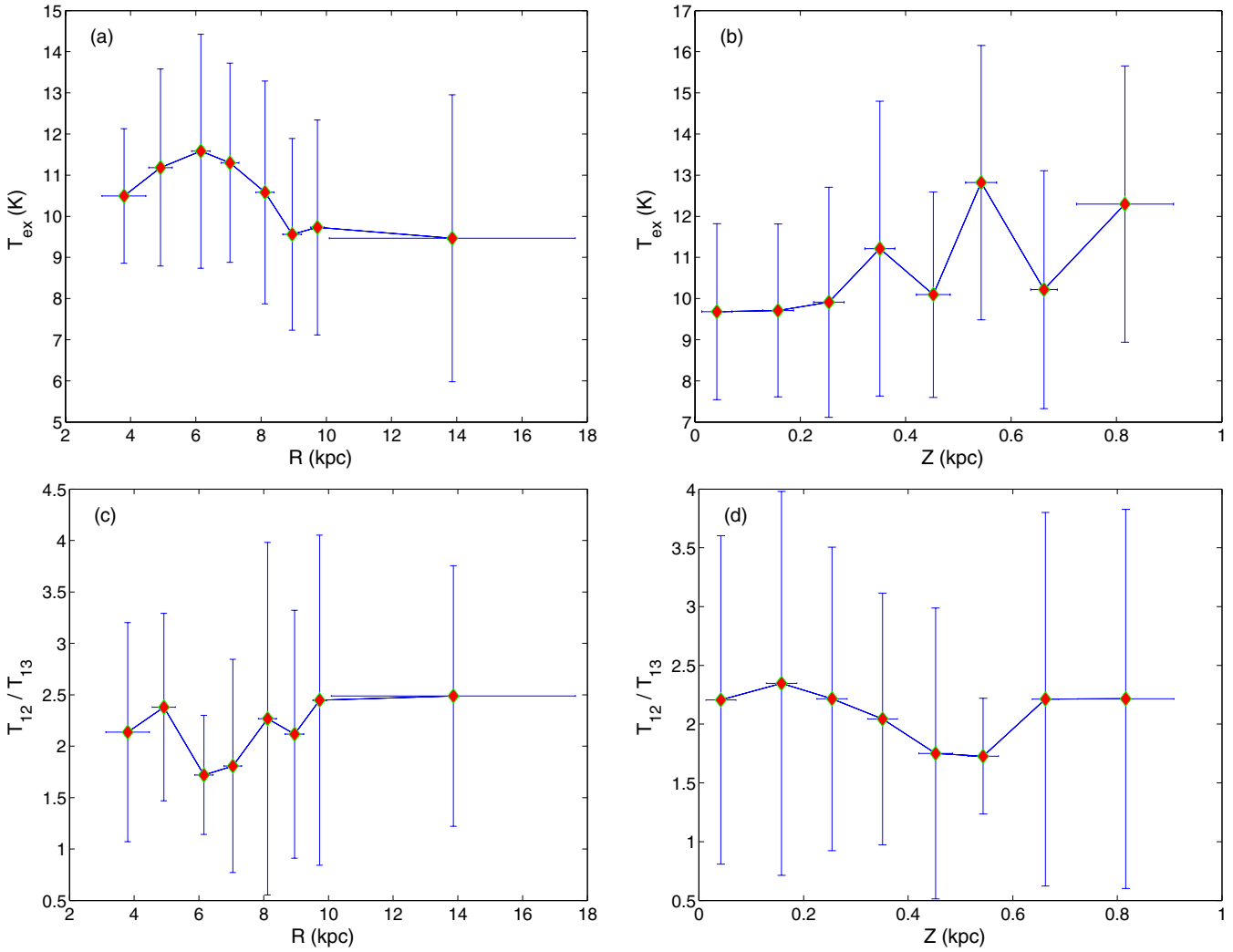


**Figure 9.** Variations of bin-averaged $T_{ex}$ and $T_{12}/T_{13}$ with distance from the Galactic center $R$ and the altitude from the Galactic disk plane $Z$. The bin size in $R$ is 1 kpc for those clumps with $R < 10$ pc and the clumps with $R > 10$ pc are put into a single bin. The bin size in $Z$ is 0.1 pc. The clumps with $Z > 1$ kpc are rare and are not included in the analysis.
(A color version of this figure is available in the online journal.)

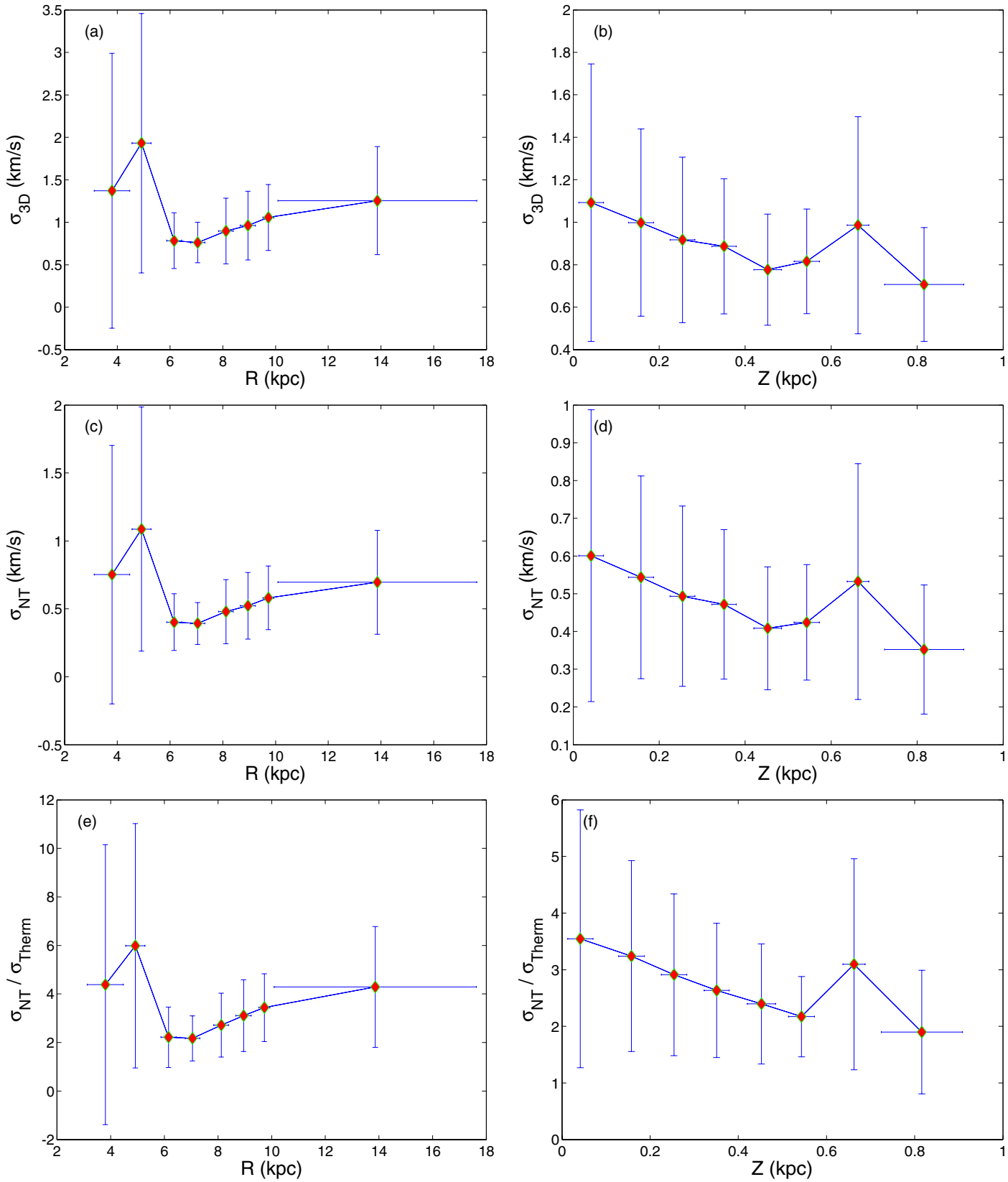


**Figure 10.** Variations of bin-averaged $\sigma_{3D}$, $\sigma_{NT}$, and the ratio of $\sigma_{NT}/\sigma_{Therm}$ of $^{13}$CO lines with $R$ and $Z$. The bin sizes are the same as for Figure 9.
(A color version of this figure is available in the online journal.)

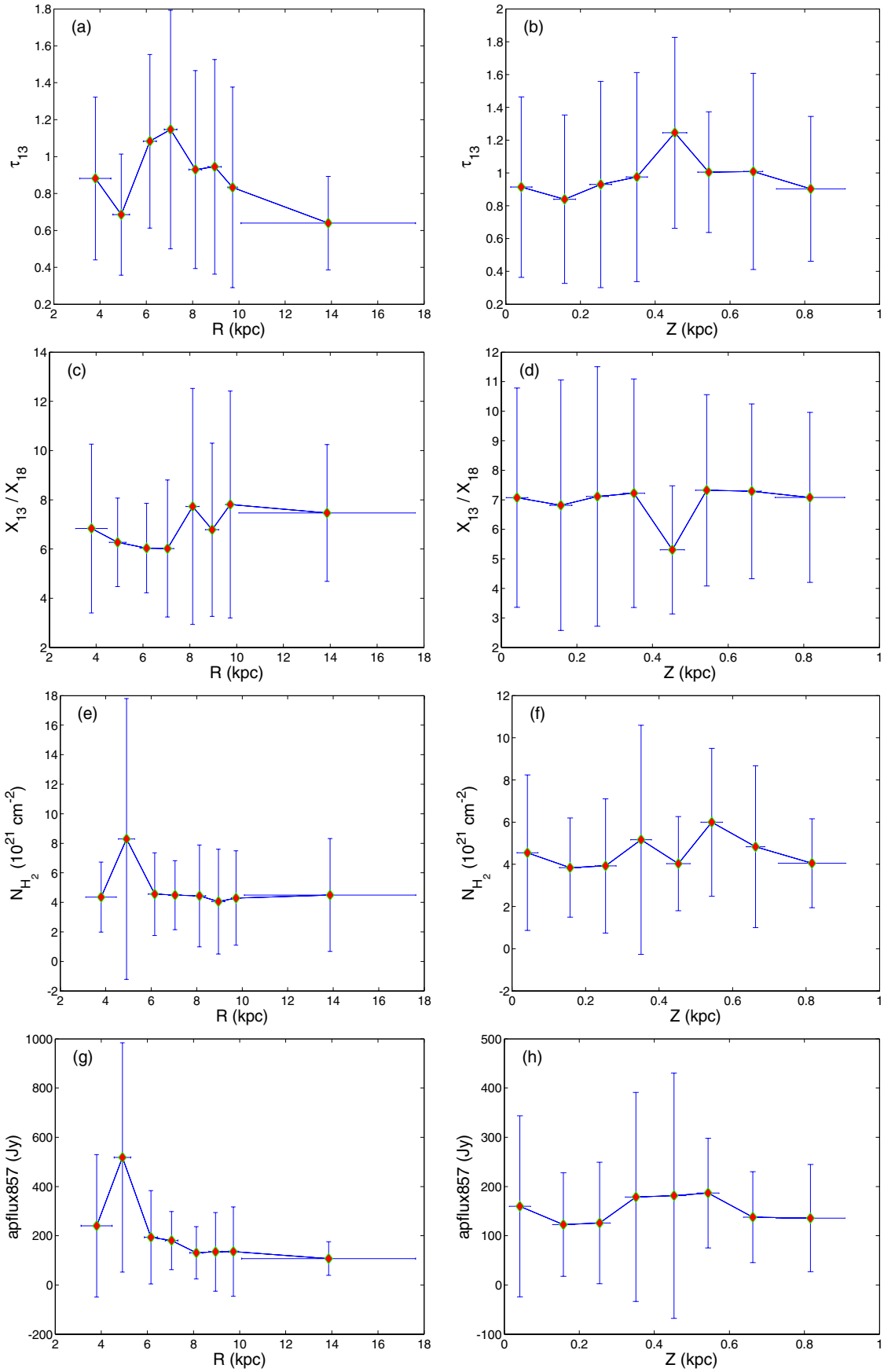


**Figure 11.** Variations of bin-averaged $\tau_{13}$, $[X_{13}]/[X_{18}]$, $N_{\rm H_2}$, and the flux at 857 GHz with $R$ and $Z$.
(A color version of this figure is available in the online journal.)

Figure 11(e) shows the radial variation of the column density of hydrogen molecules. Clearly, it presents an enhancement at 5 kpc where the densest and most massive star formation regions within our Galaxy are located. Then it is almost at a similar level until it reaches the outer region except at 9 kpc where there is a minor low valley. Owing to the small $\tau_{13}$ around 5 kpc (see Figure 11(a)) the column density is mainly affected by the velocity dispersion $\sigma_{3D}$ or $\sigma_{NT}$ shown in Figure 10. To confirm the Galactic distribution of the column density, the radial distribution of the flux density at 857 GHz dust emission detected by Planck was plotted in Figure 11(g). The variations agree with that of the column density very well. At 9 kpc the 857 GHz flux is a little higher, showing another dense structure (Scoville & Sanders 1987).

The variation of $\tau_{13}$ with altitude is shown in Figure 11(b). It exhibits a high feature between 350 and 550 pc and reaches its maximum at 450 pc. The change of the ratio of $X_{13}/X_{18}$ seen in Figure 11(d) seems to be opposite to that of $\tau_{13}$ with its lowest point at $Z = 450$ pc. Figure 11(f) presents the variation of the molecular hydrogen column density with $Z$. At $Z = 300$ and 500 pc, the values are higher than in the other regions. There is a low valley at $Z = 450$. Combining the altitude variation of $\tau_{13}$ and the velocity dispersion of Figures 10(b), (d), and (f) where $\sigma_{NT}$ is at low values, again shows that nonthermal line width is the major factor in determining the gas column density. Between 350 and 550 pc the flux at 857 GHz is higher too, which is consistent with the variation of $N_{H_2}$ as a whole. These results revealed that the column density reaches the maximum at $R = 5$ kpc, a low valley at $Z = 450$ pc, and is mainly caused by nonthermal velocity dispersion, which also has not been reported before.

#### 4.3.4. Parameters of the Clumps in Different Molecular Complexes

For the 12 complexes included in our sample, a statistical analysis of the physical parameters was made. The corresponding average values are presented in Table 2. They display different trends. The famous star formation regions including Ophiuchus, Orion, Oph-Sgr, and Taurus harbor 250 observed clumps. They have the highest excitation temperatures and column densities. The average $^{13}$CO FWHM of these clumps is less than 1.3 km s$^{-1}$. Even in Orion it is only 1.29 km s$^{-1}$, suggesting that low-mass clumps are the dominant sources in the Planck cold clumps. Their nonthermal velocity dispersion is almost two times the thermal velocity except in Ophiuchus where $\sigma_{thermal} \sim \sigma_{NT}$. Cephens harbors 87 observed clumps. The FWHM of the $^{13}$CO $J = 1$–0 line is between Orion and the above-mentioned star formation regions. $\sigma_{NT}$ is also the dominant factor for the line broadening. A common characteristic can be seen in that all four quadrants and the anticenter regions have FWHMs of the $^{13}$CO $J = 1$–0 line $\gtrsim 1.5$ km s$^{-1}$. All of them belong to the high-mass group. The $\sigma_{NT}$ is about four times the $\sigma_{thermal}$, indicating that these regions have stronger dynamic processes than other star formation regions.

### 4.4. Line Profiles

There are 16 clumps having an absorption dip at the line center, which is rather symmetric relative to the $V_{lsr}$. Nine of them show a dip in all three transitions. They may be the candidates for the $^{12}$CO depletion. In the other seven clumps, only the $^{12}$CO line has the center dips that may originate from self-absorption. Mapping is needed to further examine the properties of the line center dips. Eighteen cores with blue profiles and fifteen cores with red profiles were identified (see Table 5). Blue profiles are a kind of typical feature of molecular clump collapse (Zhou et al. 1993) whereas the red profile could originate from the expansion of the clump or outflow motion. The ratios of the clump with the blue and red profiles to the total clump numbers of clumps are small—2.7% and 2.2%, respectively. The blue excess $E = (N_b - N_r)/N_t$ is 0.004; here $N_b$, $N_r$, and $N_t$ are the clump numbers with the detected blue and red profiles and the surveyed sample (Mardones et al. 1997). $E$ of the Class -I, 0, and I clumps is 0.31, 0.30, and 0.30 shown in the HCN (3–2) line, respectively (Evans 2003), while it is 0.15–0.17 for UC H II region precursors and 0.58 for UC H II regions detected with HCO$^+$(1–0) lines (Wu et al. 2007; Fuller et al. 2005). Nevertheless, in a sample of 27 Orion starless clumps, 9 have blue profiles and 10 have red ones, implying that the blue excess $E$ is −0.04 (Velusamy et al. 2008). The ratios of the blue and red profiles to these cores are 33% and 37%, greatly exceeding those of our sample, suggesting that star formation activities occur more frequently in the Orion cores than in the Planck cold clumps. The small ratio of the blue and red profiles means that most of the Planck cold clumps do not yet have systematic star-forming motion. We also identified 19 and 13 cores with blue and red line asymmetry, respectively. Different from blue and red profiles, line asymmetry reflects the whole gas motion of the core, which may result in interaction of the core and its environment.

High velocity wings are rare in Planck cold clumps. Among the surveyed clumps, only three were detected with blue wings, six with red ones, eight with both blue and red wings, and six with a pedestal feature, showing rather rare star formation feedback activities.

### 4.5. Conditions of the Clumps at High Latitudes

There are 41 clumps located at latitudes higher than 25°. Six clumps have two velocity components and one has three. Nine of the clumps belong to the high-mass group. $T_{ex}$ is intermediate among the 12 complexes (see Table 2). The column density is $3 \times 10^{21}$ cm$^{-2}$ on average. $\sigma_{NT}$ tends to be smaller among the 12 complexes but still larger than those in the Ophiechs and Oph-Sgr. Core G089.03−41.28 has a blue profile while cores G182.54−25.34 and G210.67−36.77 have a red profile. Their altitudes are 2.4, 0.64, and 0.15 kpc, respectively, showing that star formation signatures also exist in clumps at high latitudes. Here the kinematic distance was adopted.

Since the diffuse emission was found over the whole Galactic sky (Hauser et al. 1984), many high-latitude clouds such as infrared cirrus were also detected (Low et al. 1984). Heithausen et al. (1993) made a survey for $16° \leqslant b \leqslant 44°$, $117° \leqslant l \leqslant 160°$ in the second quadrant. They found that clouds with CO emission are 13% of the survey sample. Yamamoto et al. (2003) also carried out a CO survey toward the MBM 53, 54, and 55 complex, which are within the latitude −30°–(43°). They identified 110 $^{12}$CO clouds with a total mass of 1200 $M_\odot$, in which all of the clouds are not dense enough to form stars. The conditions of our 41 Planck samples are closer to star-forming states. Additionally, the latitudes of the Planck clumps exceed those of the above samples. These results suggest that the ECC clumps are a good guide for investigating initial conditions or searching for star formation.

### 4.6. States of the 10 Mapped Clumps

The different morphologies of the contour maps of the 10 mapped clumps show that the Planck clumps contain a rather

long evolution stage, which includes diffuse and elongated regions, a filament structure or cometary shape, multiple cores, and an isolated core.

Assuming that the core is a gravitationally bound isothermal sphere with uniform density and is supported solely by random motions, the virial mass $M_{\rm vir}$ can be calculated following Ungerechts et al. (2000):

$$\frac{M_{\rm vir}}{M_\odot} = 2.10 \times 10^2 \left(\frac{R}{\rm pc}\right)\left(\frac{\Delta V}{\rm km\,s^{-1}}\right), \quad (7)$$

where $R$ is the radius of the clump and $\Delta V$ is the line width of the $^{13}$CO (1–0). The virial masses are listed in Column 14 of Table 8.

In molecular clouds, many factors including thermal pressure, turbulence, and magnetic field support the gas against gravity collapse. The Jeans mass, which takes into account the thermal and turbulent support, can be expressed as (Hennebelle & Chabrier 2008)

$$M_J \approx 1.0 a_J \left(\frac{T_{\rm eff}}{10\,\rm K}\right)^{3/2}\left(\frac{\mu}{2.33}\right)^{-1/2}\left(\frac{n}{10^4\,\rm cm^{-3}}\right)^{-1/2} M_\odot, \quad (8)$$

where $a_J$ is a dimensionless parameter of order unity which takes into account the geometrical factor, $\mu = 2.72$ is the mean molecular weight, $n = N_{\rm H_2}/2R$ is the volume density of $H_2$, and $T_{\rm eff} = (C^2_{s,\rm eff}\mu {\rm m_H}/k)$ is the effective kinematic temperature. The effective sound speed $C_{s,\rm eff}$ including turbulent support can be calculated as

$$C_{s,\rm eff} = [(\sigma_{\rm NT})^2 + (\sigma_{\rm Therm})^2]^{1/2}. \quad (9)$$

The calculated Jeans masses are listed in Column 15 of Table 8.

There are ten cores with $M_{\rm LTE}$ larger than $M_{\rm vir}$ and $M_J$, which may be under going collapse. There are also seven cores having an $M_{\rm LTE}$ that agrees with $M_{\rm vir}$ and $M_J$ within a factor of three. Considering the uncertainties in mass estimation, these cores may be in magical states. The remaining cores seem to be gravitationally unstable. One should keep in mind that these 10 clumps are not a representative sample for the whole ECC, but include the morphologies of the majority of the Planck clumps. Most of the ECC clumps show diffuse molecular emission or harbor gravitationally stable dense cores (Liu et al. 2012).

The mapped clumps are noted individually as the following.

*G001.38+20.94*. This clump is located in $\rho$ Oph. The gas emission is diffuse and it has a size >1 pc. The density is lower than $10^3$ cm$^{-3}$ and the mass >750 $M_\odot$. The excitation temperature is rather high (14 K). The average $\sigma_{\rm 3D}$ is only 0.67 km s$^{-1}$. Actually, it is located at (0.5, −1.0) with respect to L43B, a mixture of isolated globules and complexes (Benson & Myers 1989). It may be in a transition between diffuse interstellar medium (ISM) and a dense molecular cloud.

*G006.96+00.89*. This clump is located in the fourth quadrant. Two velocity components with $V_{\rm lsr}$ 9.33 and 41.67 km s$^{-1}$ were detected in the clump and both have FWHMs larger than 1.3 km s$^{-1}$. The two velocity components have four and one cores, respectively. No astronomical object was found associated with this clump so far. G006.96+00.89a, with a 9.33 km s$^{-1}$ velocity component, appears to be elongated from SE to NW and has a chain of at least four clumps. The other component has an isolated clump near the mapping center, and the clumps are not very dense with $n$ lower than $10^3$ cm$^{-3}$.

*G049.06−04.18*. This is an isolated clump and located in the first quadrant. The mass calculated with LTE is close to the Jeans and virial masses. It has been identified as CB 198 and contains IRAS 19342+1213 (J2000 = 19 36 37.8 +12 19 59) located at (8″, 43″) of the clump (Gómez et al. 2006).

*G089.64−06.59*. This is a clump in the first quadrant. Its gas clump tends to be cometary. The starless clump CB 232 AMM 1 is located at (20″, −36″) of the clump. It harbors an infrared source, IRAS 21352+4307 (Huard et al. 1999). At about 15″ eastern there is a near-infrared source, YC1-I. The LTE mass, Jeans mass, and virial mass all are close to each other.

*G108.85−00.80*. This clump belongs to the second quadrant. There are no associated objects and no known cloud was found for this clump. It shows a filamentary structure and is compact. The $^{13}$CO (1–0) line width is 2.7 km s$^{-1}$ and it is a typical high-mass clump. The LTE mass is larger than both the Jeans and virial masses. It seems very likely to be in gravitational collapse.

*G157.60−12.17*. This clump is located in the Taurus complex and has two components belonging to the L group. Contours of their integrated intensity show that the first component is rather diffuse and the second one contains two cores. TGU 1064 is located at 65″ east and south (Dobashi et al. 2005).

*G161.43−35.59*. This is a high-latitude clump and belongs to the L group. It contains at least four cores. No associated object was found.

*G180.92+04.53*. This is at the side of the anticenter of the Galaxy and belongs to the H group.

*G194.80−03.41*. The dumbbell gas emission region elongates in the northwest direction. Two large clumps are connected and each contains at least two cores. There was no associated object found. All the cores should be starless. The clump masses are all larger than the corresponding Jeans and virial masses, suggesting that they are at the gravitational bound states. TGU H1364 P8 is about 2′ away (Dobashi et al. 2005).

*G196.2−15.5*. This clump has a blue asymmetry line (see Table 6). It is associated with L1595 and a reflection nebula VDB 40 (Maddalena et al. 1986). Three cores were found in this filamentary structure. All belong to the group L. Except for the $M_J < M_{\rm LTE}$ for core 1, $M_{\rm LTE}$ is less than $M_J$ and $M_{\rm vir}$, but all these masses are close to each other.

The morphology, structure, and physical parameters of the small set of 10 mapped clumps show that Planck cold clumps cover different phases that may be (1) a transition phase from diffuse ISM to cloud, (2) a state close to gravitationally bound, (3) an isolated clump or multiple clumps, (4) starless clumps, and (5) a state that harbors infrared sources. Among the 10 clumps, 4 are in a filamentary or elongated shape which shows that filamentary clumps may be the majority in C3PO clumps. In total, 22 cores were found and 20 of these are starless.

### 4.7. Gas and Dust Coupling

The clump kinetic temperature ranges from 4 to 27 K, wider than that of dust temperatures (7–17 K; Planck Collaboration et al. 2011a). However, there are only 12 clumps with $T_k > 17$ K. The ∼98% of the clumps have $T_k \leqslant 17$ K, showing that both the dust and gas are cold and couple well. Figure 12(a) shows a comparison of the $T_d$ and $T_k$. Most of the clumps have $T_d > T_k$, indicating that gas could be heated by dust (Goldreich & Kwan 1974). For clumps with $T_d < T_k$, the gas may be due to ongoing protostellar process. For example, for the 27 clumps with $T_k > 16\,{\rm K} > T_d$, 6 are in or close to Ophiuchs, 8 in Taurus, and 10 in Orion, may be due to an ongoing protostellar process. The column densities deduced from dust emission and CO lines were plotted in Figure 12(b). One can see that the range of the values from dust is about three orders in total and that from CO

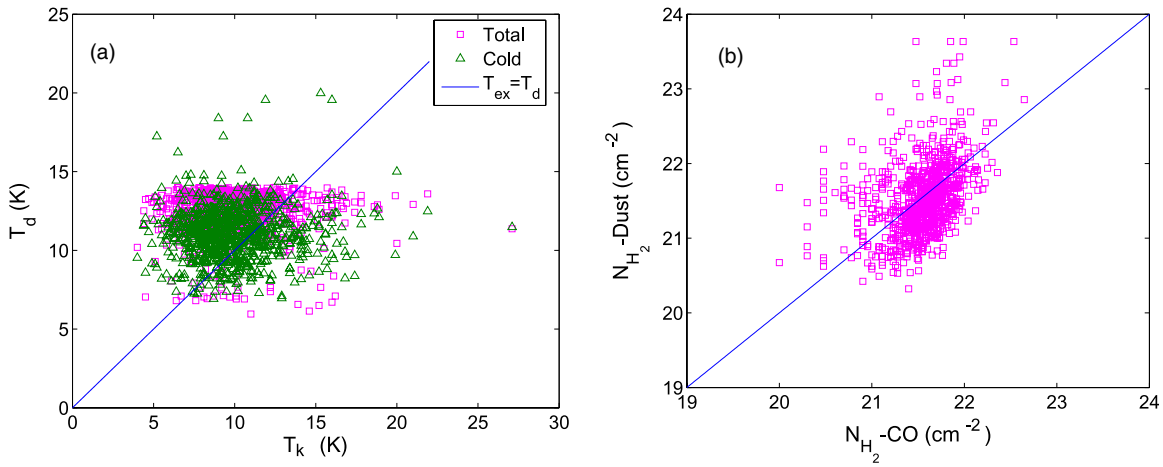


**Figure 12.** Comparison of $T_k$ to $T_d$ and $N_{H_2}$ to that deduced from dust emission.
(A color version of this figure is available in the online journal.)

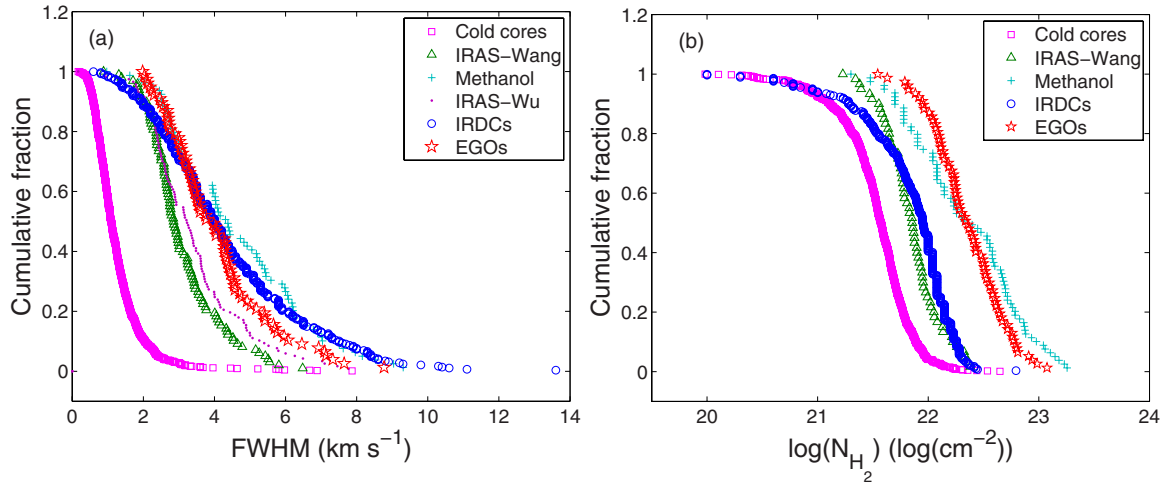


**Figure 13.** Comparisons for the cumulative fraction of the FWHM of $^{13}$CO lines and $N_{H_2}$ of different star formation samples.
(A color version of this figure is available in the online journal.)

lines is about 2.5 orders, slightly narrower. However, both the column densities concentrate on $10^{21}$–$10^{22}$ cm$^{-2}$. According to Hartquist & Williams (1998), such column density is just about the critical value of the cloud collapse.

### *4.8. Evolutional Phases—A Comparison to Different Star Formation Samples*

To investigate the physical conditions and examine the possibility of stars forming in the cold clumps, we compare the line widths of $^{13}$CO (1–0) and column densities with the following CO molecular line surveys toward different kind of targets.

1. Methanol maser sources (Liu et al. 2010),
2. Candidates of a UC H II region chosen with the *IRAS* color index and flux limit (Wu et al. 2001; Wood & Churchwell 1989),
3. Candidates of extremely young stellar objects chosen with a redder color *IRAS* index and smaller flux density than those of UC H II regions (Wang et al. 2009),
4. IRDCs (Simon et al. 2006), and
5. Extended green objects (EGOs) identified from the *Spitzer GLIMPSE* survey (Chen et al. 2010).

Figure 13(a) plots a cumulative fraction of the FWHM of $^{13}$CO (1–0). It shows that the methanol maser sources have the largest FWHMs and the smallest slopes. The IRDCs and EGOs have a shape similar to the methanol maser sources but with slightly larger slopes. When the FWHM is less than 3 km s$^{-1}$, the slope of IRDCs is almost the same as those of the UC H II candidates and the redder, weaker *IRAS* sources. When the FWHM becomes larger than 3 km s$^{-1}$, the changes of the UC H II candidates and the redder, weaker *IRAS* sources are much steeper than IRDCs, EGOs, and the methanol maser sources. The slope of the fraction of the redder, weaker *IRAS* is large and its maximum value is at 6 km s$^{-1}$. The variation of the cumulative fraction function of FWHM for the Planck cold clumps is the narrowest. The FWHM of the Planck cold clumps are the smallest compared with the other samples. For all the samples used in the comparison with Planck cold clumps, their FWHMs are almost larger than 2 km s$^{-1}$ while the cumulative fraction at FWHM $>$ 2 km s$^{-1}$ of the cold clumps is less than 10%.

The comparison of column densities for the samples of (1), (3), (4), and (5) is presented in Figure 13(b). The cumulative fraction distribution also produces the smallest column density range for the Planck cold clumps. IRDCs have nearly the same

shape as Planck cold clumps when the column density is below $10^{21}$ cm$^{-2}$, but are similar to the redder, weaker *IRAS* sources at high densities, indicating that IRDCs may be at a transition phase between Planck cold clumps and redder, weaker *IRAS* sources. The methanal maser sources and EGOs have the largest column densities, indicating active star formations in them.

These results show that the Planck cold clumps are quiescent and have the smallest column densities among these star formation samples on the whole. Most of them seem to be in transition from clouds to dense clumps.

## 5. SUMMARY

Aiming to understand gas properties of the Planck cold dust clumps, we have carried out a survey for ECC clumps with $J = 1$–0 lines of $^{12}$CO, $^{13}$CO, and C$^{18}$O. Using the 13.7 m telescope of PMO, 674 clumps were observed. Their observed parameters $V_{\rm lsr}$, FWHM, and antenna temperature were presented. Distances and physical parameters $T_{\rm ex}$, velocity dispersions, and $N_{\rm H_2}$ were derived, and their spatial distribution, regional difference, and environmental effect were investigated. Ten clumps were mapped and their morphologies and properties were analyzed. Evolutionary states of the cold clumps were discussed when compared with different star formation samples. Our main findings are as follows.

1. With the survey of the 673 clumps, 782 $^{13}$CO emission components were identified. Of these, 437 components had detection of all three transitions. Line center velocity differences for $V_{12} - V_{13}$ of 94% of the clumps and for $V_{13} - V_{18}$ of 98% of the clumps are less than $3\sigma$ of the velocity resolution. The correlations between the $V_{12}$ and $V_{13}$, $V_{13}$ and $V_{18}$ have ~100% confidence. This is the first time the agreement of the velocities of $^{12}$CO and its major isotopes, the $^{13}$CO and C$^{18}$O lines, has been confirmed with such a large sample. This suggests that the Planck clumps are quite cold and uniform as a whole and have no significant differences in dynamical or thermal material layer structures.
2. For each of the identified components, kinematic distance, galactocentric distance, and altitude from the Galactic plane were derived. The distance ranges from 0.1 to 21.6 kpc; 82% of them are located within 2 kpc and 51% of the components have distances within 0.5 and 1.5 kpc.
3. The mean value of the $^{12}$CO antenna temperature $T_{12}$ is $3.08 \pm 1.37$ K. The mean ratio of $T_{12}/T_{13}$ is $2.15 \pm 1.35$ and $T_{13}/T_{18}$ is $3.88 \pm 1.71$. Excitation temperature ranges from 3.9 to 27.0 K. Ninety-eight percent of the clumps have $T_{\rm ex}$ (or $T_k$ under LTE assumption) smaller than 17 K. A comparison of the $T_k$ and $T_d$ shows that most of the clumps have $T_d > T_k$ suggesting that gas could be heated via collision with dust and that dust and gas are coupled well in 95% of the clumps. There are clumps with $T_k > 17$ K, which are located in star formation regions such as Orion and Taurus, suggesting that the high $T_k$ is related to star-forming activities.
4. The mean FWHMs of the three transitions $J = 1$–0 lines of $^{12}$CO, $^{13}$CO, and C$^{18}$O are $2.03 \pm 1.28$, $1.27 \pm 0.77$, and $0.76 \pm 0.75$, respectively. Adopting 1.3 km s$^{-1}$ of the FWHM of the $^{13}$CO (1–0) lines as a criterion of high- or low-mass clumps, ~75% belong to the L group, suggests that the majority of the ECC clumps are low-mass clumps. For the $^{13}$CO lines the 3D velocity dispersion $\sigma_{\rm 3D}$ and nonthermal velocity dispersion $\sigma_{\rm NT}$ were calculated and we found that nonthermal the motion is the dominant line broadening.
5. Column densities of the $^{13}$CO and C$^{18}$O lines were derived. They span from $10^{14}$ to $10^{16}$ cm$^{-2}$, which is about a critical value for collapse. The ratio of $[X_{13}]/[X_{18}]$ has a mean value of $7.0 \pm 3.8$, higher than the terrestrial value. Hydrogen molecule column densities were obtained for 782 $^{13}$CO components, which are from $10^{20}$ to $4.5 \times 10^{22}$ cm$^{-2}$. Column densities derived from CO observations cover a narrower range than those deduced from dust emission.
6. Histograms for the antenna temperature $T_{12}$, the ratio of $T_{12}/T_{13}$, $T_{13}/T_{18}$, excitation temperature $T_{\rm ex}$, and the velocity dispersions ($\sigma_{\rm 3D}$, $\sigma_{\rm NT}$, and ratio of $\sigma_{\rm NT}/\sigma_{\rm therm}$) as well as $\tau_{13}$, $[X_{13}]/[X_{18}]$, and $N_{\rm H_2}$ were fitted with a lognormal distribution. The distributions of line widths of the three transitions, $T_{13}/T_{18}$, $T_{\rm ex}$, $\sigma_{\rm 3D}$, $\sigma_{\rm NT}$, $\sigma_{\rm NT}/\sigma_{\rm therm}$, and $[X_{13}]/[X_{18}]$ can be well depicted purely by a lognormal distribution. The lognormal distribution of the $H_2$ column density is with a long tail which is consistent with those found in active star-forming regions, indicating that some of the Planck cold clumps reside in star-forming regions. We suggest the distributions of line widths or velocity dispersions are more likely to reflect the effect of supersonic turbulence in clouds.
7. Physical parameter variations in Galactic space were investigated. As a variation with radius the hydrogen molecule column density reaches maximum at $R \sim 5$ kpc, which is consistent with the 857 GHz flux density. However, $\tau_{13}$ decreases to a low valley while the $\sigma_{\rm NT}$ or $\sigma_{\rm 3D}$ reaches a peak. The results suggest that the velocity dispersion of the molecular line is the dominant factor in determining the column density. Velocity dispersions decrease as the altitude increases and they reach their lowest point at $Z = 450$ pc. Although $\tau_{13}$ is at its highest value here, the column density is at a low valley, further conforming that nonthermal line broadening plays a major role in exciting the molecular transition.
8. Line profile characteristics including a possible depletion dip, blue and red profiles, as well as high velocity wings were found in part of the clumps, indicating star-forming activities. However, the number of these clumps is less than 10% of the whole sample, indicating that star formation is not yet active in Planck cold clumps.
9. Parameters in different molecular complexes in our Galaxy show different scores. Clumps in the molecular complexes Ophiuchus, Taurus, and Orion show high excitation temperatures while those in the first–fourth quadrants have larger velocity dispersions.
10. Ten mapped cold dust clumps have very different gas emission morphologies, showing filaments or elongated structures. Twenty-two gas cores were identified with sizes of a tenth to 5 pc, densities from $10^2$ to $10^3$ cm$^{-3}$ and masses from dozens to thousands of $M_\odot$. Ten cores seem to be in a gravitationally bound state.
11. Planck cold clumps are the most quiescent ones among the samples of weak red *IRAS*, UC H II candidates, IRDCs, EGOs, and methanol maser sources, suggesting that the Planck cold clumps are at a very early phase in cloud evolution.

This work is a preliminary investigation for Planck cold clumps. Mapping observations are necessary for obtaining the properties of the Planck clumps. Various molecular species, especially dense molecular tracers, are needed for examining

dense clumps and star formation processes in the ECC clumps. Mapping with H I line in ECC clumps is useful to investigate the transition from diffuse to dense ISM.

We are grateful to the staff at the Qinghai Station of PMO for their assistance during the observations. We thank the Key Laboratory for Radio Astronomy, CAS, for partial support in the operation of the telescope. This work was supported by China Ministry of Science and Technology under State Key Development Program for Basic Research (2012CB821800).

## REFERENCES

Bally, J., & Lada, C. J. 1983, ApJ, 265, 824
Benson, P. J., & Myers, P. C. 1989, ApJS, 71, 89
Bergin, E. A., Ungerechts, H., Goldsmith, P. F., et al. 1997, ApJ, 482, 267
Beuther, H., Schilke, P., Menten, K. M., et al. 2002, ApJ, 566, 945
Cesaroni, R., Walmsley, C. M., & Churchwell, E. 1992, A&A, 256, 618
Chen, X., Shen, Z.-Q., Li, J.-J., Xu, Y., & He, J.-H. 2010, ApJ, 710, 150
Clark, F. O., & Johnson, D. R. 1981, ApJ, 247, 104
Clemens, D. P. 1985, ApJ, 295, 422
Dame, T. M., Hartmann, D., & Thaddeus, P. 2001, ApJ, 547, 792
Dame, T. M., Ungerechts, H., Cohen, R. S., et al. 1987, ApJ, 322, 706
Dobashi, K., Uehara, H., Kandori, R., et al. 2005, PASJ, 57S, 1
Du, F. J., & Yang, J. 2008, ApJ, 686, 384
Egan, M. P., Shipman, R. F., Price, S. D., Carey, S. J., & Clark, F. O. 1998, ApJ, 494, L199
Evans, N. J., II. 2003, in Chemistry as a Diagnostic of Star Formation, ed. C. L. Curry & M. Fich (Ottawa: NRC Press), 157
Evans, N. J., II, Beckwith, S., & Blair, G. N. 1977, ApJ, 217, 448
Froebrich, D., Murphy, G. C., Smith, M. D., Walsh, J., & Del Burgo, C. 2007, MNRAS, 378, 1447
Fuller, G. A., Williams, S. J., & Sridharan, T. K. 2005, A&A, 442, 949
Garden, R. P., Hayashi, M., Hasegawa, T., Gatley, I., & Kaifu, N. 1991, ApJ, 374, 540
Goldreich, P., & Kwan, J. 1974, ApJ, 189, 441
Gómez, J., de Gregorio-Monsalvo, I., Suárez, O., & Kuiper, T. B. H. 2006, AJ, 132, 1322
Goodman, A. A., Pineda, J. E., & Schnee, S. L. 2009, ApJ, 692, 91
Guilloteau, S., & Lucas, R. 2000, in ASP Conf. Ser. 217, Imaging at Radio through Submillimeter Wavelengths, ed. J. G. Mangum & S. J. E. Radford (San Francisco, CA: ASP), 299
Hartquist, T., Caselli, P., Rawlings, J., Ruffle, D., & Williams, D. 1998, in the Chemistry of Star Formation Regions, the Molecular Astrophysics of Stars and Galaxies, ed. T. Hartquist & D. Hartquist (Oxford: Clarendon), 101
Harvey, P. M., Campbell, M. F., & Hoffmann, W. F. 1977, ApJ, 211, 786
Harvey, P. M., Smith, B. J., di Francesco, J., & Colome, C. 1998, ApJ, 499, 294
Hauser, M. G., Gillett, F. C., Low, F. J., et al. 1984, ApJ, 278, L15
Heithausen, A., Stacy, J. G., de Vries, H. W., Mebold, U., & Thaddeus, P. 1993, A&A, 268, 265
Hennebelle, P., & Chabrier, G. 2008, ApJ, 684, 395
Huard, T. L., Sandell, G., & Weintraub, D. A. 1999, ApJ, 526, 833
Juvela, M., Ristorcelli, I., Montier, L. A., et al. 2010, A&A, 518, L93
Juvela, M., Ristorcelli, I., Pagani, L., et al. 2012, A&A, 541A, 12
Kainulainen, J., Beuther, H., Henning, T., & Plume, R. 2009, A&A, 508, L35
Liu, T., Wu, Y., & Wang, K. 2010, Res. Astron. Astrophys., 10, 67
Liu, T., Wu, Y., & Zhang, H. 2012, arXiv:1207.0881
Low, F. J., Young, E., Beintema, D. A., et al. 1984, ApJ, 278, L19
Maddalena, R. J., Morris, M., Moscowitz, J., & Thaddeus, P. 1986, ApJ, 303, 375
Mardones, D., Myers, P. C., Tafalla, M., et al. 1997, ApJ, 489, 719
Molinari, S., Brand, J., Cesaroni, R., & Palla, F. 1996, A&A, 308, 573
Muller, S., Beelen, A., Guélin, M., et al. 2011, A&A, 535, 103
Myers, P. C., & Benson, P. J. 1983, ApJ, 266, 309
Myers, P. C., Linke, R. A., & Benson, P. J. 1983, ApJ, 264, 517
Planck Collaboration, Ade, P. A. R., Aghanim, N., Arnaud, M., et al. 2011a, arXiv:1101.2035
Planck Collaboration, Ade, P. A. R., Aghanim, N., Arnaud, M., et al. 2011b, A&A, 536A, 22
Planck Collaboration, Ade, P. A. R., Aghanim, N., Arnaud, M., et al. 2011c, A&A, 536, 19
Planck Collaboration, Ade, P. A. R., Aghanim, N., Arnaud, M., et al. 2011d, A&A, 536, 23
Qin, S.-L., Huang, M., Wu, Y., Xue, R., & Chen, S. 2008, ApJ, 686, L21
Rathborne, J. M., Jackson, J. M., & Simon, R. 2006, ApJ, 641, 389
Ridge, N. A., Di Francesco, J., Kirk, H., et al. 2006, AJ, 131, 2921
Scoville, N. Z., & Sanders, D. B. 1987, in Interstellar Processes, ed. D. J. Hollenbach & H. A. Thronson (Dordrecht: Reidel Publishing Company), 21
Sharpless, S. 1959, ApJS, 4, 257
Simon, R., Rathborne, J. M., Shah, R. Y., Jackson, J. M., & Chambers, E. T. 2006, ApJ, 653, 1325
Snell, R. L., Loren, R. B., & Plambeck, R. L. 1980, ApJ, 239, L17
Sridharan, T. K., Beuther, H., Saito, M., Wyrowski, F., & Schilke, P. 2005, ApJ, 634, L57
Sridharan, T. K., Beuther, H., Schilke, P., Menten, K. M., & Wyrowski, F. 2002, ApJ, 566, 931
Strom, K. M., Strom, S. E., Carrasco, L., & Vrba, F. J. 1975, ApJ, 196, 489
Strom, S. E., Vrba, F. J., & Strom, K. M. 1976, AJ, 81, 314
Ungerechts, H., Umbanhowar, P., & Thaddeus, P. 2000, ApJ, 537, 221
Vázquez-Semadeni, E. 1994, ApJ, 423, 681
Velusamy, T., Peng, R., Li, D., Goldsmith, P. F., & Langer, W. D. 2008, ApJ, 688, L87
Wang, K., Wu, Y., Ran, L., Yu, W. T., & Miller, M. 2009, A&A, 507, 369
Watson, A. M., Coil, A. L., Shepherd, D. S., Hofner, P., & Churchwell, E. 1997, ApJ, 487, 818
Wood, D. O. S., & Churchwell, E. 1989, ApJ, 340, 265
Wu, Y., Henkel, C., Xue, R., Guan, X., & Miller, M. 2007, ApJ, 669, L37
Wu, Y., Wu, J., & Wang, J. 2001, A&A, 380, 665
Wu, Y., Zhang, Q., Yu, W., et al. 2006, A&A, 450, 607
Yamamoto, H., Onishi, T., Mizuno, A., & Fukui, Y. 2003, ApJ, 592, 217
Zhang, S. B., Yang, J., Xu, Y., et al. 2011, ApJS, 193, 10
Zhou, S., Evans, N. J., II, Koempe, C., & Walmsley, C. M. 1993, ApJ, 404, 232